Interaction of a rigid buoyant sphere and a deforming bubble with a vortex ring: The role of deformability

Subhajit Biswas [*] and Raghuraman N. Govardhan [†]
Department of Mechanical Engineering, Indian Institute of Science, Bangalore 560012, India

(Received 19 May 2022; accepted 13 September 2022; published 29 September 2022)

In bubbly turbulent flows, the deformation of the bubble is known to play an important role in the interaction between the carrier phase and the dispersed phase. In the present paper, we experimentally study an idealized version of the problem where we look at the interaction of a deforming air bubble (nonzero Weber number) and a rigid buoyant particle (zero Weber number) with a single vortex ring (in water) for a large range of ring-circulation-based Reynolds numbers ($\mathrm{Re} = \Gamma/\nu$=6000–67 300; Γ=ring circulation, ν=kinematic viscosity of water). We are able to obtain the particle to fluid density ratio ($\rho_{\mathrm{particle}}/\rho_{\mathrm{water}} \approx 0.008$) to be very low and of the same order as that of the bubble ($\rho_{\mathrm{bubble}}/\rho_{\mathrm{water}} \approx 0.001$), with the main difference being the distinct difference in their deformability. The buoyant low density (rigid) particle and the deforming bubble are directly engulfed into the core of the vortex ring and enable measurements of the effects of particles or bubbles on the vortex ring. On the particle (and bubble) dynamics side, distinct differences can be seen right from the capture phase, as unlike the rigid particle, the bubble undergoes a large axial elongation and, consequently, a quicker capture than the particle. After capture by the ring, the bubble experiences an azimuthal pressure gradient, which leads to its elongation into a thin long bubble whose diameter is relatively small compared to the vortex core size. In sharp contrast, the particle does not deform and remains effectively localized along the rings azimuthal direction. These differences in the shape of the bubble and particle within the ring lead to distinct differences in the ring's convection speed, azimuthal vorticity, and enstrophy at later times. In particular, the measurements indicate that the localized large perturbation to the vorticity in the rigid particle case (an equivalent of a rigid bubble, zero Weber number) leads to a larger disruption of the vortex ring as seen in terms of higher reduction in the rings convection speed and azimuthal enstrophy than for the deforming bubble (nonzero Weber number) case. These results could have implications in bubbly turbulent flows such as in bubble drag reduction (BDR), where many studies [like Van Gils *et al.*, J. Fluid Mech. **722**, 317 (2013)] indicate that deforming bubbles are better for drag reduction than nondeforming bubbles at higher flow Re, where the dominant mechanism is the lifting of structures away from the wall. The present results suggest that in cases where vortex disruption is the primary mechanism for BDR [for example, at lower flow Re, Sugiyama *et al.*, J. Fluid Mech. **608**, 21 (2008)], better drag reduction would occur with nondeforming bubbles. The current study thus brings us insight into the role of deformability in the interaction of bubbles with a vortical structure, which could be important in helping us model and understand bubble-turbulence interactions.

DOI: 10.1103/PhysRevFluids.7.094302

[*] subhajitb@iisc.ac.in, sbiswas.iisc@gmail.com, https://mecheng.iisc.ac.in/fpl/.
[†] rng@iisc.ac.in, https://mecheng.iisc.ac.in/fpl/.

I. INTRODUCTION

Turbulent dispersed multiphase flows are common in numerous engineering and environmental applications and have been studied for decades (Balachandar and Eaton [1]). Typical examples of such flows are the dispersion of particles or bubbles in chemical reactors, bubbles at the ocean surfaces and mixing layers, dispersed pollutants in the atmosphere, and when bubbles are injected into a water boundary layer for drag reduction. In these flows, the presence and deformation of bubbles or particles can have a dramatic influence on the mass, momentum and energy transfer of the continuous phase flow fields and vice versa (see, for example, Refs. [1–4]). Although the turbulence modulation by the dispersed phase has been carried out by several researchers, as discussed in many reviews [1,2,5], the mechanisms behind turbulence modulation are not completely understood due to the complex nature of the interaction among the primary and the dispersed (secondary) phases. In their review article, Balachandar and Eaton [1] stated that *"mechanisms of turbulence modulation and their parametric dependence are poorly understood and are wide open for fundamental investigation."* They suggested that to improve our understanding of these turbulent dispersed flows, experimental techniques proficient in yielding simultaneous measurements of both the carrier and dispersed phases (bubbles or particles) should be developed and need to be used for further investigations. Driven by this motivation and the often discussed role of bubble deformability in the interactions, in the present paper, we experimentally study an idealized version of the problem where we look at the interaction of a deforming air bubble and a rigid buoyant particle (an equivalent of a rigid bubble) with a single vortex ring (in water), with the broad focus being on understanding the role of the bubble's deformability in these interactions.

In bubbly turbulent flows, the deformation (and breakup) of bubbles is known to play a critical role in the mass, momentum, and energy transport between the primary (carrier) phase and the bubbles [1,6]. In these flows, the deformation and possible breakup of a bubble, as discussed in many studies [7,8], depends on the potential of the hydrodynamic forces exerted by the surrounding fluid to deform the bubble against surface tension forces [8]. Several studies have also investigated the role of deforming and nondeforming bubbles on the dynamics of the local and the instantaneous properties of flow turbulence [6,9,10]. For example, in vertical channel bubbly turbulent flows, Lu and Tryggvason [6] and Dabiri *et al.* [10] reported differences in bubble void fraction distribution between deformable and rigid bubbles, and they attributed this to bubble deformation causing differences in the lift force on the bubble [11]. Also, they reported differences in the carrier phase flow turbulence modulation between deforming and nondeforming bubbles. For example, Bunner and Tryggvason [9] in their direct numerical simulation (DNS) study of bubbles in a homogeneous turbulent vertical channel shear flow reported larger velocity fluctuations in the carrier phase fluid by deforming bubbles than (nearly) rigid bubbles. These studies clearly show that the bubble's deformability could significantly affect the overall characteristics of the flow. Nondeforming bubbles in a bubbly turbulent flow are important in a few different contexts (studies). These include numerical studies where the interactions with nondeforming bubbles are investigated using the point bubble approach [12,13], cases where the bubbles are very small (low Weber numbers) [14,15], and in van den Berg *et al.* [16] due to the actual presence of buoyant rigid particles in Taylor-Couette flow.

Several studies have investigated the effects of bubbles on the integral properties of turbulence, such as the structure-function, acceleration *probability density function*, energy redistribution, and scaling laws [17,18]. Mazzitelli *et al.* [17] in their study on the effect of microbubbles (nondeforming) on the distribution of energy at different scales in the flow reported a reduction in energy at the large scales and an increase at the small scales induced by the bubbles interacting with vortices. In free shear flows, for example, in a bubbly mixing layer, as reported by Climent and Magnaudet [19], the presence of bubbles (nondeforming) could significantly affect the large-scale coherent structures present in the flow, which in turn causes meandering of the large-scale structures in the lateral direction and an increase in the rate of spreading of the mixing layers. One practical application of bubble injection in turbulent shear flows is drag reduction [3,5,20]. Murai [5] and Van Gils *et al.* [21] discussed several possible mechanisms involved in bubble drag reduction (BDR)

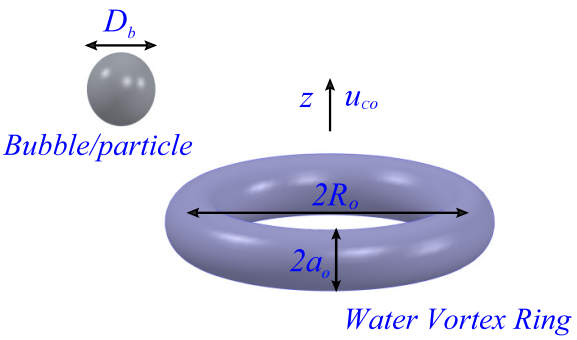

FIG. 1. A schematic of a bubble (and buoyant particle) of diameter D_b and a vortex ring of diameter $2R_o$ and core diameter of $2a_o$, traveling vertically upward in z direction with velocity u_{co}.

in turbulent shear flows, including (i) nondeforming bubbles disrupting and breaking the coherent structures [12,22,23], (ii) nondeforming bubbles introducing effective compressibility of the flow [24], and (iii) deforming bubbles pushing the near-wall high vorticity region away from the wall [16,21,25]. As discussed by Murai [5], depending on the flow Re, bubble size, and other conditions, one mechanism could dominate over the other(s). For example, in Taylor-Couette flows, at low Re, the mechanism for BDR is disruption of the large-scale structures [12,23,26] by bubbles. On the other hand, at large Re, the primary mechanism is related to bubble deformability [16,21], as the deforming bubbles push the near-wall high vorticity regions away from the wall [25], caused by changes in the lift force on the bubble due to its deformation [27].

Turbulent flow consists of eddies or vortices of various length scales [28], with these vortical structures playing a fundamental role in turbulence. Hence, to understand bubbly turbulent flows, it is useful to focus on the effects of bubbles on the dynamics of these vortical structures. In bubbly turbulent flows, the interplay of bubbles with turbulent structures can be seen as many bubbles interacting with a large set of vortical structures, making such interactions quite complex to understand. Hence, driven by the motivation to understand the role of bubbles' deformability on turbulence modulation, in the present paper, we study an idealized version of the problem by investigating the interaction of a *deforming air bubble* and a buoyant rigid particle (*a rigid bubble*) with a single water vortex ring (see Fig. 1), with the broad focus being on understanding the role of bubble's deformability and nondeformability in vortex ring-bubble interactions.

A few studies have reported the effects of bubbles or solid particles on a vortex ring. Sridhar and Katz [29] reported that a few microbubbles could distort the vortex ring core, with the core returning to its initial state after the bubbles escape. The circulation was found to be almost constant, with about a 20% rise in the core's peak vorticity. Cihonski *et al.* [30] performed a *DNS* of the Sridhar and Katz [29] configuration and showed that the bubble-induced reaction force on the liquid is very small and hence unable to distort the core. The numerical simulation by Finn *et al.* [31] of bubble entrainment and interaction with a 2D vortex found vortex decay by the bubble-induced local reaction forces. Ferrante and Elghobashi [32], in their numerical simulations on minute microbubble interactions with a Taylor-Green vortex, observed bubbles settling in the core's high enstrophy region, causing vorticity reduction due to positive local divergence and enstrophy reduction in the highest enstrophy region. More recently, Jha and Govardhan [33] and Biswas and Govardhan [34–36] experimentally investigated a vortex-ring interaction with single and multiple bubbles, respectively. At low Weber number (We), they reported fragmentation of the vortex core, a large reduction in ring convection speed, azimuthal enstrophy, and peak vorticity, while the circulation remained broadly conserved. Very recently, Foronda-Trillo *et al.* [37] numerically investigated the effects of bubble to vortex-size ratio and Weber number on the breakup of an air bubble that is

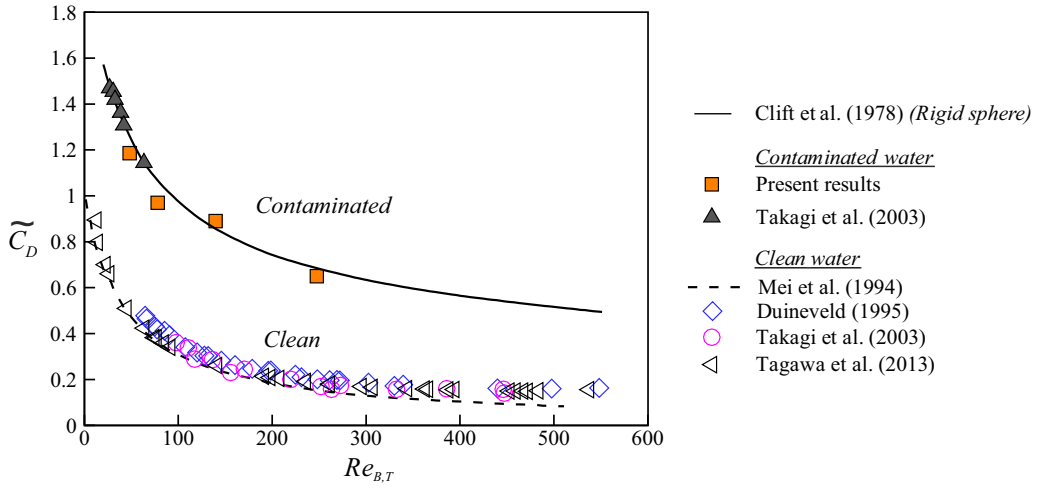

FIG. 2. Drag coefficient ($\widetilde{C_D}$) of freely rising bubbles (for bubble diameter < 1.5 mm): A comparison is shown between the present results in tap water (contaminated) with an empirical relation for a rigid sphere from Clift *et al.* [48], experimental results for contaminated bubbles (Takagi *et al.* [49]), numerical results for a clean bubble (Mei *et al.* [52]), and experimental results for clean bubbles (Takagi *et al.* [49], Duineveld [50], Tagawa *et al.* [51]).

colliding with a transitional vortex ring. In their 3D simulation, they reported reduction in azimuthal enstrophy after interaction with the bubble, although the overall enstrophy remained nearly constant.

On the vortex-ring interaction with solid particles, very few studies have been reported so far. For example, Uchiyama and Yagami [38] numerically studied collision between a gas vortex ring and small glass particles that are considerably heavier than the gas. In this process, the strength and convection velocity of the vortex ring was found to be reduced. Domon *et al.* [39] experimentally studied the transport of solid particles by a vortex ring, and observed reduction in the convection speed of the vortex ring compared to the no-particle case, and they speculated that this was due to changes in the ring's properties.

In the present paper, we experimentally investigate the similarities and differences between the interaction of a single deforming bubble with a vortex ring and that of a single buoyant rigid spherical particle (*an equivalent of a rigid bubble*; surface tension, $\sigma \to \infty$) with a single vortex ring. In both cases, the bubble (and particle) size (D_b) is of the order of the ring core diameter ($D_b/2a_o \approx$ 0.8 to 1.4; a_o=vortex core radius), and the ring has a nondimensional core radius (a_o/R_o; R_o=vortex ring radius) of about 0.2, considered to be a thin core vortex ring [40]. The present experiments are carried out in tap water, and thus, the air-liquid interface may effectively be considered to correspond to the no-slip boundary condition due to the presence of impurities (see Fig. 2). We are experimentally able to obtain the density ratio of the rigid particle ($\rho_{\text{particle}}/\rho_{\text{water}} \approx 0.008$) to be very small and close to the deforming air bubble ($\rho_{\text{bubble}}/\rho_{\text{water}} \approx 0.001$). Although there is a difference between the two cases, the variation in density is small compared to the displaced fluid density (0.7% of fluid density), and a quick calculation of the buoyant energy contribution to the ring from the bubble and particle as a percentage of the ring energy [41] indicates that they are relatively small (about 9% even at the lowest ring Re of 6000), with a small variation (0.7%) between the bubble and particle. Hence, we feel that it will not lead to any significant differences in the ring dynamics during the interactions. Therefore, the main difference between the bubble and the particle cases studied would be the deformability of the bubble.

In these interactions, the parameters quantifying the vortex ring include the ring radius (R_o), its core radius (a_o) being represented in terms of the nondimensional core thickness (a_o/R_o), and

the ring circulation (Γ)-based Reynolds number, $\mathrm{Re} = \Gamma/\nu$ (ν=kinematic viscosity). On the bubble (particle) side, it is the *rigid buoyant* spherical particle's diameter and the *deforming* bubble's equivalent diameter D_b. In terms of the ring-bubble (particle) interactions, the coupled parameters are the bubble (particle) to ring core volume ratio [$V_R = (\pi D_b^3/6)/(2\pi^2 R_o a_o^2)$] or the bubble (particle) to ring core diameter ratio ($D_b/2a_o$), and ring-circulation-based Weber number (We), defined along the lines of Choi *et al.* [42], as $\mathrm{We}=\Delta P/(\sigma/D_b)$, where $\Delta P = 0.87\rho_{\mathrm{water}}(\Gamma/2\pi a_o)^2$ is the pressure difference between the vortex core center and the ambient and σ is the surface tension ≈ 0.072 Nm^{-1}. In the present paper, the bubble (particle) to ring core volume ratio (V_R) was varied between 0.02 to 0.1 corresponding to $D_b/2a_o$ values between 0.8 and 1.4, although the main focus of the paper is on the $D_b/2a_o$ of the 1.4 case.

In bubbly turbulent flows, the strength of the vortical structures can vary considerably, and hence, in the present paper, the vortex ring strength in terms of its circulation (Γ)-based Re is varied. It should be noted that the interaction of a vortex ring with a rigid buoyant particle corresponds to a nondeforming bubble with We=0, while the case of a deforming bubble corresponds to $\mathrm{We} > 0$. In particular, we focus our attention on the differences between the two cases to help us understand the importance of bubble deformability on the interaction processes between the bubble and the ring, including the capture dynamics, the postcapture dynamics within the ring, and from the vortex ring side, on the ring diameter's growth, its deformation, propagation speed, azimuthal vorticity, and azimuthal enstrophy. In this paper, we directly contrast the interaction of a rigid and deformable bubble with a vortical structure.

The layout of this paper is as follows. In Sec. II, we discuss the experimental setup and methodologies adopted to measure different aspects of the bubble and particle dynamics and vortex ring dynamics. Following this, in Sec. III, we contrast the bubble and particle capture dynamics and their motion within the vortex core. In Sec. IV, from the vortex ring dynamics side, we discuss the differences and similarities between the effects of bubble and particle on the ring's propagation speed, ring diameter, deformation of the ring quantified by the ring's aspect ratio, modulation of the vortex core azimuthal vorticity distribution including integral measures of it such as the circulation and azimuthal enstrophy. The conclusions from the paper are then summarized in Sec. V.

II. EXPERIMENTAL METHODS

For the studies, a vortex ring was generated in a transparent water tank (see Fig. 3) by impulsively pushing a slug of water through a ring generator (a circular nozzle) with a diameter (D_G) of 15 mm using a piston-cylinder arrangement (for details, see Jha and Govardhan [33]). The nondimensional piston stroke length L_P/D_G was always kept lower than 4 to avoid any trailing jet [43] (L_P is the piston stroke length). The vortex rings thus formed had a relatively thin core with a nondimensional core radius (a_o/R_o) of about 0.2 (a_o=core radius, R_o=ring radius) (see Table I). The generated ring traveled vertically upward with a circulation strength (Γ), which was varied by changing the piston velocity profile to obtain a wide range of ring Re ($= \Gamma/\nu$) of 6000–67 300, covering laminar, transitional, and turbulent regimes [44]. The ring was characterized by its circulation (Γ), ring radius (R_o), and core radius (a_o), all obtained from time-resolved particle image velocimetry (PIV) measurements (for details of PIV measurements, refer to Refs. [33,34]). Vortex ring circulation (Γ) was measured using the surface integral of azimuthal vorticity ($\int \omega\, dA$) taken over a surface enclosed by a large closed loop enclosing the vortex core. The radius of the vortex ring (R_o) and its core (a_o) were found from the vertical component of velocity measured along a horizontal line joining the center of both cores (Sullivan *et al.* [45]) after the complete formation of the vortex ring. All the experiments reported here were performed after the vortex ring was fully formed.

The deforming bubble and buoyant particle were released adjacent to the vortex ring generator with both the bubble and particle interacting with the ring as they convected vertically upward. The bubble (particle) studied had a diameter (D_b) of approximately 5.7 mm (in most of the cases), with the particle being spherical and the bubble having an equivalent diameter of 5.7 mm, as estimated from size measurements from different views. Studies were also done with smaller D_b

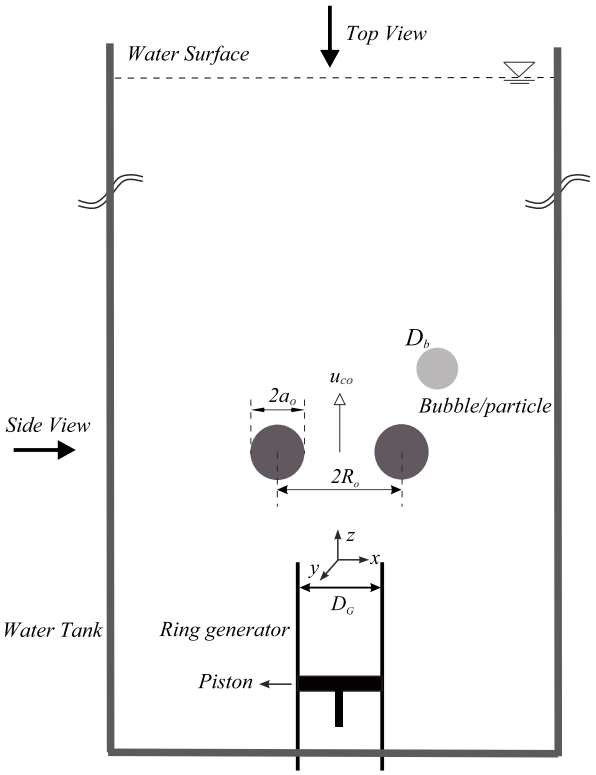

FIG. 3. Schematic of the side view of the present experimental setup for a single bubble (particle) interacting with a vortex ring. A piston-cylinder arrangement was used to generate the vortex ring and a bubble (and buoyant particle) was released near the vortex ring. The vortex having a diameter $2R_o$ and core diameter $2a_o$, while convecting upward with a convection speed of $u_{\rm co}$, captures the bubble (particle) with diameter D_b. The dynamics of the interactions were recorded from both the side- and top-view visualizations.

of 4.4 mm and 3.1 mm to investigate the effects of bubble (particle) size on the interactions. Before conducting experiments on the interaction of the vortex ring and the bubble, the bubble size was measured independently from zoomed-in visualizations of the bubble immediately after its pinch-off. From these experiments, the (equivalent) spherical bubble diameter (D_b) was calculated from measurements taken in two perpendicular planes. This (equivalent) bubble diameter was then averaged over multiple runs to obtain the nominal equivalent spherical bubble diameter (D_b). This equivalent diameter was found to differ by less than 2% between different runs. After release, the buoyant bubble (particle) moved upward and was subsequently pulled into the vortex ring core

TABLE I. Table shows different nondimensional numbers before interacting with a bubble (particle).

Re	a_o/R_o	$D_b/2a_o$	V_R	$We_{\rm particle}$	$We_{\rm bubble}$
6000	0.19	1.47	0.12	0	12
13 200	0.19	1.47	0.12	0	46
25 800	0.20	1.41	0.11	0	160
39 900	0.22	1.36	0.10	0	321
56 700	0.22	1.36	0.10	0	601
67 300	0.22	1.36	0.10	0	763

due to the low pressure within the core, and the interaction begins. It may be noted here that in these interactions, the modulations in the vortex ring dynamics and bubble dynamics depends on the strength of the vortex ring ($\mathrm{Re} = \Gamma/\nu$) and on the bubble to vortex size ratio ($D_b/2a_o$), and both these effects are studied in the present paper. All the bubble sizes studied in the present paper fall nominally in the wobbly bubble regime (Tripathi *et al.* [46]) for a freely rising bubble case. However, in the present interaction cases, the nominal bubble regime in free rise does not seem to be important, as the results indicate that the bubble is rapidly pulled in toward the low-pressure ring core, with this resulting in the deformation of the bubble into a well-defined bullet-shaped nearly axisymmetric form. During the capture process, and later within the ring, the dynamics of the bubble is thus mainly governed by the relatively strong effects that the ring has on the bubble and not by the bubble regime in the free rising bubble case. The experiments were carried out in tap water, where, due to the presence of impurities, the air-liquid interface may effectively be considered to correspond to the no-slip boundary condition (Magnaudet and Eames [27], Takagi and Matsumoto [47]). Before conducting experiments on ring-bubble (particle) interactions, the effective boundary condition at the air-water interface (for the bubble) was checked by measuring the drag coefficient of freely rising small bubbles in the tap water used for the experiments. This was done by releasing small bubbles with equivalent diameters smaller than 1.5 mm in the same water, and the resulting drag coefficients ($\widetilde{C_D}$) obtained from measured terminal velocities are shown in Fig. 2 as a function of the bubble Reynolds number ($\mathrm{Re}_{B,T}$). Also shown in the plot is the empirical relation for a rigid sphere (Clift *et al.* [48]), results for bubbles in contaminated water (Takagi *et al.* [49]), bubbles in clean water (both experimental (Duineveld [50]; Takagi *et al.* [49]; Tagawa *et al.* [51]), and numerical (Mei *et al.* [52])). The comparison shows that the present results clearly lie along the contaminated water (rigid sphere) drag line and are very distinct from the drag on bubbles in clean water. This indicates that due to contamination present in the tap water used, the boundary condition at the air-water interface (for the bubble) can be regarded as a no-slip one like on a rigid sphere. However, in the ring-bubble interactions, the bubble is free to deform during the interactions as seen in the visualizations in the following section. In the case of the buoyant particle, a low relative density was a critical requirement, and this was achieved by making the particle from expanded polystyrene material, which has a density of approximately 8 $\mathrm{kg/m^3}$, and as required does not deform during the interactions with the ring. It may be noted that the surface tension of the tap water used was measured and found to be approximately 0.072 $\mathrm{Nm^{-1}}$ at room temperature.

The main nondimensional parameters in this paper are the ring-circulation-based Weber numbers (We), defined along the lines of Choi *et al.* [42], as $\mathrm{We}{=}\Delta P/(\sigma/D_b)$, the bubble (particle) to ring core volume ratio [$V_R = (\pi D_b^3/6)/(2\pi^2 R_o a_o^2)$] and bubble (particle) to ring core diameter ratio ($D_b/2a_o$) (see details in Table I), where $\Delta P = 0.87\rho_{\mathrm{water}}(\Gamma/2\pi a_o)^2$ is the pressure difference between the vortex core and the ambient and $\sigma = 0.072$ $\mathrm{Nm^{-1}}$ is the surface tension of water. As seen in Table I, although there are variations caused by ring Re and its effects on the core size (a_o), broadly $D_b/2a_o$ and V_R are kept approximately fixed at 1.4 and 0.1, respectively, corresponding to the D_b of the 5.7 mm bubble (particle) case. The different stages of the ring-bubble (-particle) interactions were captured by high-speed imaging of the side view using shadowgraphy and through direct imaging of the top view of the interactions, both using a Photron SA5 camera. These views were captured separately due to different illumination requirements, after ensuring that the broad features remain repeatable and similar. During these interactions, to visualize the ring, microbubbles were generated through electrolysis at the vortex generator tip, with these microbubbles being seen in Fig. 4. These bubbles were much smaller then the millmeter-sized main bubble (particle) of diameter D_b and the core radius a_o, and therefore their impacts on the broad features of the ring are expected to be negligible. This was also verified by comparing the convection speed of the ring measured using the microbubbles with a separate set of measurements done using dye visualizations, and no perceivable difference in convection speed was found due to the presence of the microbubbles. Also, to verify that the tracer microbubbles were reasonably close to the vortex core center, the distance between the left and right core centers was measured using PIV (in the absence of microbubbles) and compared with the one measured from the visualizations

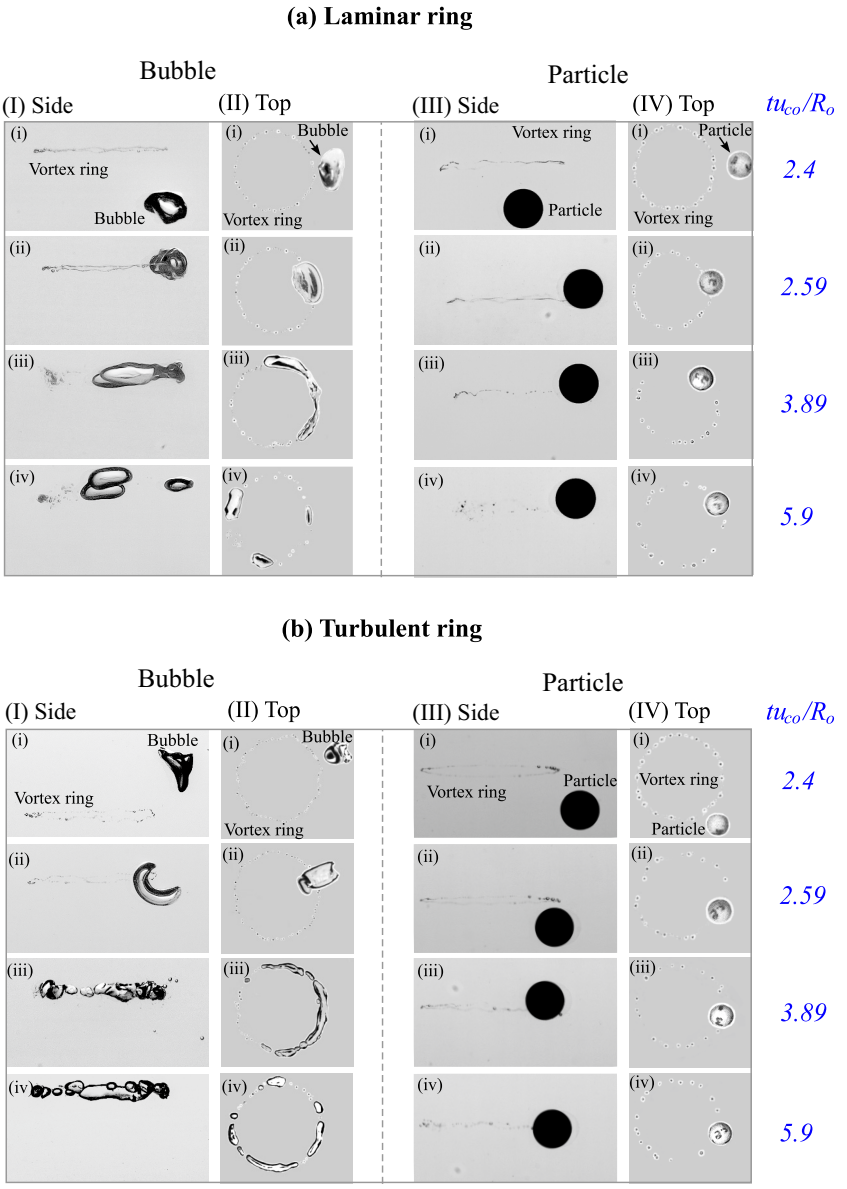

FIG. 4. Time sequence of images of the side view and top view visualizations of a bubble (particle) interacting with a single (a) laminar (Re=6000), and (b) turbulent (Re=25 800) vortex ring. As seen in the figure, the bubble undergoes large elongation before and after capture by the ring and breaks into several smaller bubbles within the ring. On the other hand, as expected, the rigid particle does not deform. Here, the nondimensional times (tu_{co}/R_o) corresponding to the instances shown are (i) 2.4, (ii) 2.59, (iii) 3.89, and (iv) 5.9, respectively. In all cases shown, $D_b/2a_o \approx 1.4$.

with microbubbles. Again, no perceivable difference was found between these two measurements, indicating that the position of these microbubbles do reasonably represent the core center. The velocity and vorticity fields were obtained by time-resolved PIV (TRPIV) at a high repetition rate using a LDY-301 laser (for details, see Ref. [33]). The initial convection speed of the vortex ring (u_{co}) and the initial ring radius (R_o) just before capture of the particle (bubble) were used to normalize the

dimensional time (t), the ring's vertical position (z), and the azimuthal vorticity (ω). For each of the experiments with and without a bubble (particle), a minimum of three repetitions of the experiments were carried out, and the average value of these is shown in plots in the following sections, along with vertical bars to indicate the variation between the runs.

III. BUBBLE (PARTICLE) DYNAMICS

In this section, we present and contrast the bubble dynamics and particle dynamics during their interactions with the vortex ring. This include the process of bubble (particle) capture by the ring and, postcapture, their motions within the ring for a large range of vortex ring Re (≈6000 to 67 300). We begin by presenting in Fig. 4 the high-speed imaging of a typical interaction of a deforming bubble (We > 0) and a rigid buoyant particle (a nondeforming bubble, We=0) with a laminar [Re=6000 in Fig. 4(a)] and a turbulent vortex ring [Re=25 800 in Fig. 4(b)]. Both cases correspond to $D_b/2a_o \approx 1.4$, which is the focus of the present paper, with the effect of variations in $D_b/2a_o$ being discussed later in Sec. IV E (Fig. 14). In each case, both the side view and top view of the interactions are shown to give a better feel of the interactions. These two views are captured separately due to different illumination requirements after making sure that the broad features remain the same. We now directly focus on contrasting the bubble and the particle dynamics in their interactions with the vortex ring. In Fig. 4, in both the laminar (Re=6000) and turbulent (Re=25 800) ring-bubble (-particle) interaction cases, the first image in the sequence shows the bubble (particle) outside the ring, with the subsequent images showing the capture of the bubble (particle) by the vortex ring due to the low pressure within the vortex core. It may be noted here that, although there is a possibility that the initial position of the bubble (particle) is also a parameter, our experimental results indicate that irrespective of the initial position of the bubble (particle), the vortex ring dynamics remain broadly the same from the instant of bubble (particle) capture by the ring. The time of capture of the bubble (particle) by the ring is, however, dependent on the initial location due to the larger distance that the bubble (particle) has to travel, and hence the capture time discussed in the next subsection does have a well-defined initial radial location ($3a_o$) to enable uniform comparison across cases. The fact that the initial location is not important may also be seen from the model for the capture time of a bubble (particle) by a thin vortex ring (discussed in the next subsection), where due to the negligible inertia of the bubble (particle), there is effectively a radial force balance between the inward pressure force and the outward drag force that completely determines the radial bubble (particle) velocity at any given radial location, irrespective of the initial bubble (particle) location.

Now, the fact that the buoyant low density (rigid) particle and (deforming) bubble are directly captured by the vortex ring enables measurements of the effects of the particle and bubble on the vortex ring. During the capture phase and, subsequently, within the vortex ring, the bubble deformation is apparent in the bubble case, with it being stretched axially before capture and azimuthally after capture within the ring, the latter due to the pressure gradients within the core after capture (Jha and Govardhan [33]). This azimuthal bubble elongation within the ring after capture leads to the formation of a long thin bubble thread along the core. On the other hand, as expected, the rigid particle before and after capture does not deform, although the capture happens in a qualitatively similar way due to the comparatively low relative density of the buoyant particle. Unlike the bubble elongating and breaking within the ring postcapture, the rigid particle does not deform and remains effectively localized along the rings azimuthal direction. Also, looking at the top-view visualization images, it is clear that as the ring strength (Re) is increased, the number of broken bubbles also increases. During the ring-bubble (-particle) interactions, these differences in the shape of the bubble and the particle lead to distinct differences in the ring convection speed, azimuthal vorticity, and enstrophy, and will be discussed in the following section. During this entire ring-bubble (-particle) interaction time, while the ring convects vertically upward (z) with a convection speed of u_c, the velocity and vorticity fields are obtained from PIV at a high repetition

rate. In this section, we present and contrast the bubble dynamics and particle dynamics during their interactions with the vortex ring.

A. Bubble (particle) capture

In bubbly turbulent flows, the preferential concentration of bubbles is governed by the probability of capture of these bubbles by the vortical regions, which in turn would decide the interaction between these bubbles and vortices, and the modulation of the global flow properties. Balachandar and Eaton [1] in their review discuss the preferential concentration of particles, droplets, and bubbles in turbulent flows and their importance in determining the dynamics of the carrier phase flow, and state that there have been relatively fewer experimental studies of the preferential concentration of bubbles compared to particles and hence recommend further investigations. Driven by this motivation, in the present paper, along with bubble-induced modulation of a vortex in the next section, we also investigate the effects of bubble's deformability on the bubble capture process of the vortex ring.

In the conceptually simple configuration of vortex-bubble interactions, the dynamics of bubble capture by a vortex has been discussed by a few previous studies [31,33,53]. In the present paper, we directly focus on the contrast between the capture of a deforming bubble and a rigid particle (rigid bubble) to understand the effects of a bubble's deformability on the capture process. As mentioned earlier, in both the bubble and particle cases in our study, the ratio of the bubble (particle) diameter to the core diameter ($D_b/2a_o$) is maintained to be approximately 1.4. As seen in Fig. 4, the interaction between the vortex ring and the bubble (particle) begins with its capture by the ring. As the bubble (particle) comes close to the vortex ring, the low pressure within the vortex core induces a motion of the bubble (particle) that leads to their spiraling motion into the vortex core, as seen in Figs. 4(a) and 4(b). During this process, unlike the particle that remains undeformed, the bubble experiences a large elongation as seen in Figs. 4(a)(I)(ii) and 4(b)(I)(ii), and the bubble reaches a radial position within the vortex core, where it is in radial equilibrium, with any subsequent motion (deformation) being restricted only to the azimuthal direction.

An important quantity related to the capture process is the bubble (particle)'s capture time (t_c) and, in the present context, we compare the capture times of a deforming bubble and nondeforming particle, the latter being relatively unstudied in the literature. Here, the capture time is defined as the time the bubble (particle) takes to travel from $r = 3a_o$ to $r \approx a_o/2$, where r is the radial location of the bubble center from the center of the vortex core similar to the definition in Oweis *et al.* [53]. Here, the reference radial location r=0 is taken at the center of the core. We experimentally measure this capture time (t_c) from time sequences of the bubble (particle) visualization (as in Fig. 4) for different ring Reynolds numbers. This is summarized in Fig. 5(a) by showing the radial location (r/a_o) of the bubble (particle) as a function of time for a laminar (Re=6000) and turbulent (Re=25 800) ring, and in both cases, the deforming bubble is seen to move more rapidly to the center of the vortex core, with the capture time (t_c) in the deforming bubble cases being roughly half of the nondeforming (particle) value in both the laminar and turbulent ring cases. In Fig. 5 and the subsequent figures in the paper, rigid particle ($\boldsymbol{P}$) and deforming bubble ($\boldsymbol{B}$) are subscripted by L and T, and these represent a laminar (Re=6000) and a turbulent (Re=25 800) ring case, respectively.

To get a broader view of the contrast in capture times (t_c) of the bubble and the particle, the normalized capture times ($t_c u_{co}/R_o$) of the bubble and particle are shown in Fig. 5(b) for all the Re cases studied, with the variation between repetitions of experiments shown by the uncertainty bars. We can see that the capture time for the particle is considerably larger than the deforming bubble in all the Re cases studied. The smaller capture time of the deforming bubble is due to the axial deformation of the bubble during the capture, which leads to a smaller drag on the deforming bubble than the rigid particle. Further, as seen in the figure, it is clear that in the deforming bubble case, $t_c u_{co}/R_o$ reduces considerably with increasing Re, due to the larger axial deformation of the bubble during its capture phase at higher ring strengths (ring Re) as seen in the (side view) visualizations of

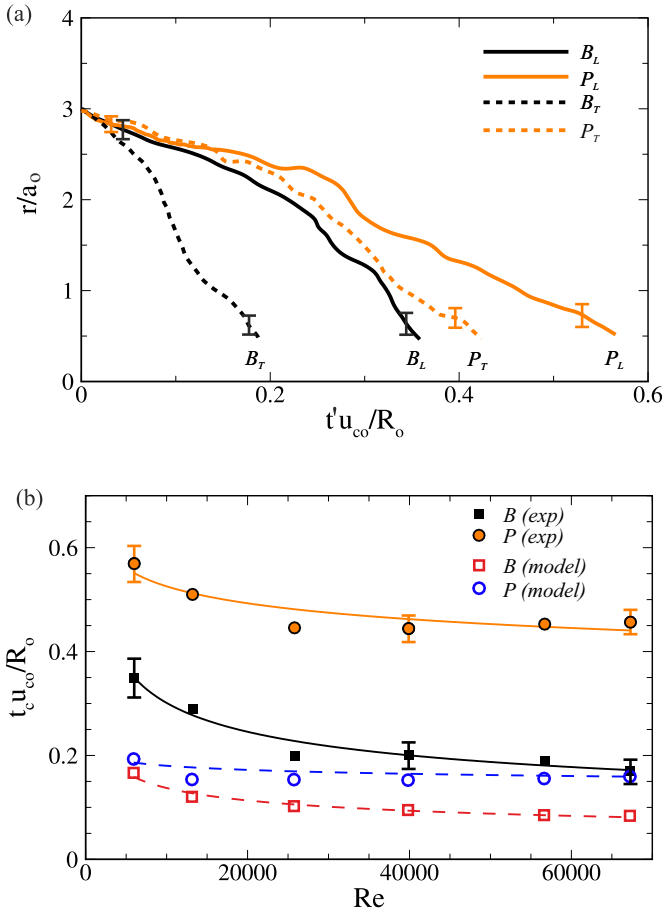

FIG. 5. (a) The nondimensional radial distance (r/a_o) of the bubble (particle) from the vortex core center with time ($t'u_{co}/R_o$) as the bubble (particle) travels from r/a_o=3 to $r/a_o \approx 1/2$, shown for a laminar (Re=6000) and turbulent (Re=25 800) ring; here, t' is the dimensional time and is taken to be zero when the bubble (particle) is at r/a_o=3. (b) The variation of the nondimensional capture time ($t_c u_{co}/R_o$) with ring Re for the particle and bubble cases. The capture time computed from a simplified model initially proposed by Oweis *et al.* [53] is also shown. In this figure and subsequent figures in the text, rigid particle (***P***) and deforming bubble (***B***) are subscripted by *L* and *T*, and these represent a laminar (Re=6000) and a turbulent (Re=25 800) ring case, respectively.

the interaction. In contrast, in the particle case, the reduction in $t_c u_{co}/R_o$ with increasing Re is very small and is related purely to the direct Re effect, as there is no deformation.

A simple model for the capture time of bubble (particle) may be obtained from a radial force balance model as proposed by Oweis *et al.* [53]. In this model, the capture time is computed from a radial force balance between the drag force (F_D) resisting the inward radial motion and the pressure gradient induced inwards pull (F_P) on the bubble (particle). In the force balance, the bubble (particle) acceleration and the shear lift force are neglected, as these are small compared to F_P and F_D due to bubble's (particle's) low density and the negligible vorticity outside the vortex core, respectively. Therefore, the radial force balance on the bubble (particle) simplifies to the balance between the pressure gradient induced force (F_P) and the drag force (F_D) on the bubble (particle). Further, with the additional assumption that the largest component of bubble (particle) velocity is in the radial

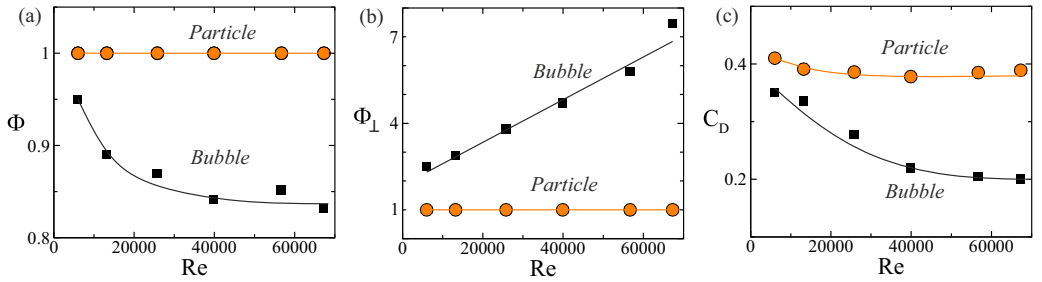

FIG. 6. The variation of the (a) sphericity Φ and (b) crosswise sphericity $\Phi_\perp$, with ring Re for deforming bubble and rigid particle cases. (c) The drag coefficient (C_D) variation with ring Re for the spherical particle and elongated bubble cases during their capture process, obtained from the expressions of Haberman and Morton [54] and Hölzer and Sommerfeld [55], the latter based on the measured elongated shape.

direction ($u_{b,r}$), the radial force balance can be expressed as

$$\frac{\rho u_\theta^2 V_b}{r} = \frac{1}{2}\rho C_D\left(\frac{\pi}{4}\right)D_b^2 u_{b,r}^2. \tag{1}$$

In the above expression [Eq. (1)], u_θ is the bubble's (particle's) azimuthal velocity, and V_b is the volume of the bubble (particle). In the present case, as we have a relatively thin vortex core, its azimuthal velocity (u_θ) may be approximated by the induced velocity of a line Gaussian vortex. The bubble's (particle's) radial velocity ($u_{b,r}$) may be obtained from the above radial equilibrium equation, taking care to use an appropriate expression for C_D of the bubble (particle), which is valid over the range of bubble (and particle) Reynolds numbers ($\mathrm{Re}_b = u_{b,r}D_b/\nu$) experienced during the capture process. To find the capture time (t_c) from the model, we perform an integration of the obtained radial velocity ($u_{b,r}$) from bubble's (and particle's) initial radial location of $r = 3a_o$ to $r{=}a_o/2$. In Oweis *et al.* [53] and Jha and Govardhan [33], the C_D for a bubble was obtained from standard expressions for the drag on a sphere at low (Stokes drag [48]) and at moderate Re [54].

As seen in the present visualizations for the deforming bubble earlier, the bubble shape can be far from spherical and, hence, the drag force based on a sphere is not really valid for a deformed bubble. Therefore, to account for this deformation of the bubble, we use an expression for C_D of an elongated particle from Hölzer and Sommerfeld [55] given as

$$C_D = (8/\mathrm{Re}_b)(1/\sqrt{\Phi_\perp}){+}(16/\mathrm{Re}_b)(1/\sqrt{\Phi}){+}(3/\sqrt{\mathrm{Re}_b})(1/\Phi^{3/4}){+}0.4210^{0.4(-\log\Phi)^{0.2}}(1/\Phi_\perp), \tag{2}$$

where Φ and $\Phi_\perp$ are the sphericity and crosswise sphericity of the elongated bubble during the capture process. The sphericity (Φ) is defined as the ratio of the surface area of the volume equivalent spherical bubble to the surface area of the elongated bubble, and the crosswise sphericity ($\Phi_\perp$) is the ratio of the cross-sectional area of the volume equivalent spherical bubble and the projected cross sectional area of the elongated bubble [55], both evaluated from visualizations of the bubble capture process at each of the ring Re cases studied. In Figs. 6(a) and 6(b), the variation of Φ and $\Phi_\perp$ are shown with ring Re, for both the elongated bubble and the spherical particle. For the particle, both Φ and $\Phi_\perp$ are 1, as it remains spherical in shape. While, for the bubble, these changes with increasing ring Re are due to the increasing deformation (elongation) of the bubble, and consequent reduction in C_D. On the other hand, the C_D for the nondeforming spherical particle (rigid bubble) is purely dependent on the Re and is obtained over the required Re range using the expression [Eq. (3)] from Haberman and Morton [54]:

$$C_D = (24/\mathrm{Re}_b)(1 + 0.197\mathrm{Re}_b^{0.63} + 0.00026\mathrm{Re}_b^{1.38}). \tag{3}$$

These expressions for C_D of both the particle (We=0) and the deforming bubble (We >0) are valid for the entire range of bubble (and particle) Reynolds number (Re_b) in the present paper.

To evaluate the Reynolds number of the bubble (particle) (Re_b) during their capture phase, their velocity during the capture phase was obtained from the side-view images (as in Fig. 4). To compare the C_D of particle (We=0) and bubble (We > 0), the C_D values obtained from the above-mentioned standard expressions [Eqs. (2) and (3)] are shown with ring Re in Fig. 6(c). We can see that the C_D of the elongated bubble (We >0) is significantly smaller than that of the particle (We=0) that is approximately 0.4 over the range of ring Re studied. In contrast, for the deforming bubble, C_D is significantly smaller than a particle and found to be varying with ring Re due to the bubbles increasing axial deformation with ring Re. For example, $C_D \approx 0.35$ at Re=6000 and $C_D \approx 0.2$ at Re=67 300.

In Fig. 5(b), the capture time obtained from the model ($t_{c,\mathrm{model}}$) is plotted with Re, and we can see that there is a significant reduction in $t_{c,\mathrm{model}}$ with increasing Re for the deforming bubble (We > 0). This decrease in $t_{c,\mathrm{model}}$ is due to the reduction in C_D of the deforming bubble leading to its smaller capture time. On the other hand, for the rigid particle (We=0), as we can see in Fig. 6, the C_D remains nearly the same at all Re, and hence, the capture time obtained from the model remains relatively constant with increasing Re. In Fig. 5(b), it can be noticed that although the model correctly shows a significantly reduced capture time for the deforming bubble compared to the rigid particle, it should be noted that there is a considerable difference in capture time between the model and the experimentally measured values. This is likely due to several factors such as the effects of added mass and lift forces that become more important as the bubble (and particle) approach the vortex core (Oweis *et al.* [53]), besides the fact that the bubble (and particle) modify the core vorticity distribution.

The above observations in our idealized study indicate that in bubbly flows there would be a significantly faster capture of deforming bubbles in vortical regions than nondeforming bubbles leading to differences in their preferential distribution. This in turn could result in differences in the global flow properties in deforming and nondeforming bubbly flows in terms of the bubble-flow interactions and bubble-bubble interactions (such as bubble coalescence).

B. Bubble (particle) dynamics within the vortex ring

We shall now proceed to discuss and compare the dynamics of the bubble and particle within the vortex ring subsequent to the capture process. We have already seen in Fig. 4 that postcapture, the bubble elongates azimuthally due to the azimuthal pressure gradient [33] within the core, in contrast to the particle that remains undeformed. From the top-view visualizations, such as Figs. 4(a)(II) and 4(b)(II), the bubble's elongation information as a function of time are obtained until the time the first breakup of the azimuthally extended bubble occurs. The elongated bubble length (L_b^*) is shown with time in Fig. 7(a); here, $L_b^* = L_b/2\pi R'$, where L_b and $2\pi R'$ are the instantaneous bubble azimuthal length and the rings instantaneous perimeter, respectively. As we can notice in Fig. 7(a), at ring Re of 25 800, the elongation is higher and faster at later times compared to the ring with Re of 6000. In the case of the particle, as expected, no elongation occurs and L_b^* remains constant at $L_b/2\pi R' = D_b/2\pi R' \approx 0.08$ in the given experiment.

During a bubble's elongation within the vortex ring, the bubble surface develops Rayleigh-Plateau instability, and the elongated thread after reaching a critical aspect ratio [56] starts breaking at multiple azimuthal locations, producing many smaller bubbles. These broken bubbles produced from the elongated bubble thread can undergo further breakup until at later time the breakup process is completed. In Fig. 7(b), the number of broken bubbles (N_b) as a function of time ($t u_{co}/R_o$) is shown at two-ring Reynolds numbers (Re=6000, 25 800). We start by looking at the case of the laminar Re of 6000, where the elongated bubble undergoes binary breakup. At this Re, these broken bubbles stay azimuthally, sufficiently far apart within the vortex core, and the broken bubbles in some cases experience a further binary split that results on average in about three broken bubbles at larger times. At higher ring Reynolds numbers, for example, in the turbulent Re=25 800 case, the elongated bubble thread undergoes breakup at multiple (>3) azimuthal locations, and we can see that the main bubble breaks (N_b increases) into a relatively larger number of broken bubbles,

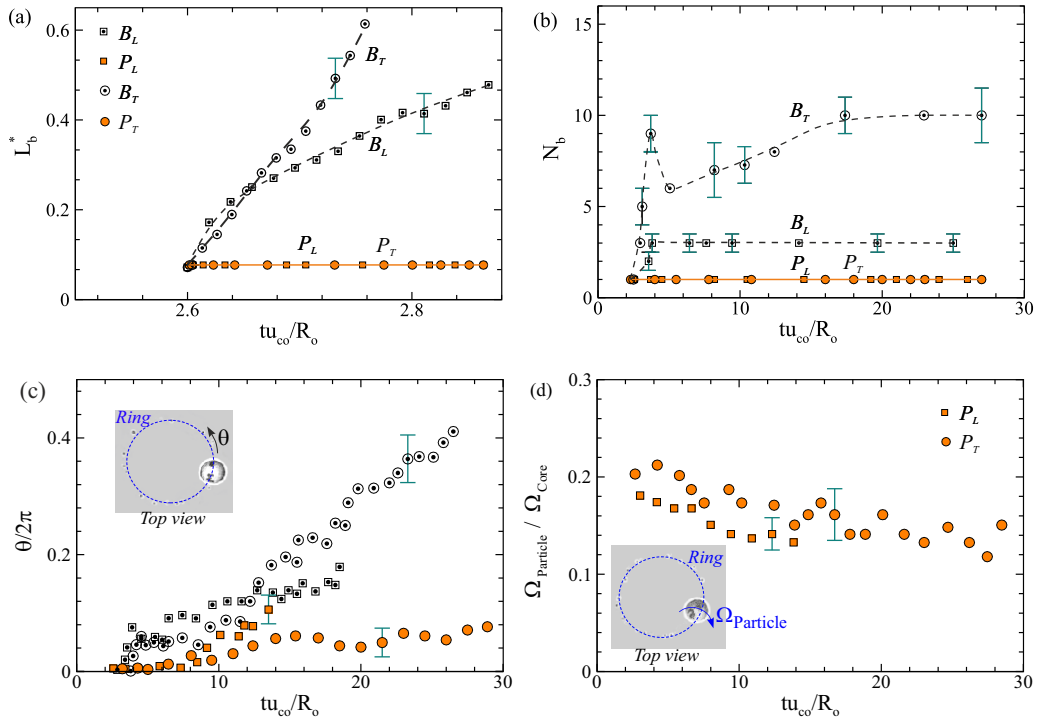

FIG. 7. (a) Bubble's nondimensional azimuthal elongation (L_b^*) inside the vortex with nondimensional time (tu_{co}/R_o), shown for a laminar (Re=6000) and turbulent (Re=25 800) ring; here, $L_b^* = L_b/2\pi R'$, where L_b is the instantaneous bubble's elongated length and $2\pi R'$ is ring's instantaneous perimeter. Here, rigid particle ($\boldsymbol{P}$) and deforming bubble ($\boldsymbol{B}$) cases are subscripted by $\boldsymbol{L}$ and $\boldsymbol{T}$, and these represent the laminar and turbulent cases, respectively. (b) The number of broken bubbles (N_b) inside the vortex ring shown with nondimensional time (tu_{co}/R_o). (c) The translation of the rigid particle and a broken bubble along the azimuthal direction (θ) with time (tu_{co}/R_o). (d) The variation in the rate of rotation of the particle (Ω_{particle}) normalized by the average angular rotation rate of the core [Ω_{core}] is shown with time (tu_{co}/R_o). In (c) and (d), top-view images of a particle within the vortex ring are attached for a better demonstration of the translational and rotational motions.

and these can undergo further breakup and coalescence (N_b decreases at some times). Finally, after sufficient time, the breakup is complete and a large number of smaller broken bubbles remain within the vortex core, with the final broken bubble numbers being significantly higher than in the lower Re (laminar) case, as seen in Fig. 7(b). Now, these broken bubbles within the ring drift azimuthally and spread to cover a large azimuthal extent, about 80–100% of the ring, whereas the particle remains intact and slowly drifts azimuthally by about 10–20% of the ring's circumference. Hence, a particle (We=0) acts like a localized large perturbation to the ring, while a deforming bubble (We $>$ 0) acts as a more distributed perturbation to the ring. We shall see that this difference has a profound impact on the time evolution of the perturbed vortex ring due to capture of the bubble (particle) in the next section.

Within the vortex ring, the broken bubbles and the rigid particle undergo azimuthal drift and this is measured from the top view imaging of the interaction. The azimuthal (θ) translation of the particle and a (broken) bubble with time (tu_{co}/R_o) is shown in Fig. 7(c) along with a top view image of a particle within a ring attached for a better illustration. In Fig. 7(c), θ=0 represents the particle capture location along the vortex ring's azimuthal axis, while for the broken bubble, it is taken to be the azimuthal location where the broken bubble is produced from the breakup of an elongated bubble thread within the ring. As can be seen in the figure, compared to the particle, a broken bubble

undergoes comparatively larger azimuthal drift, while the particle remains more localised within the vortex ring with relatively small azimuthal drift. Now, another interesting quantity to look at is the rotation of the bubble and the particle within the ring, as we know that during their azimuthal drift, they will be expected to undergo rotational motion. Similar to translational motion, from the top-view imaging of the interactions, the rate of rotation of the particle can be easily measured, while in the case of a bubble, its rotation is not easy to capture and hence is not presented here. The top view of the interaction shows that the particle undergoes rotation (Ω_{particle}) about a rotational axis passing through its center and parallel to the ring's azimuthal axis; see the top-view image of Fig. 7(d) for a better representation. In the figure, the rotation rate of the particle after normalising by the average angular rotation rate of the core (Ω_{core}) is shown with time (tu_{co}/R_o). As we can see, there is a reduction in the rate of rotation with time, and this is possibly due to the weakening of the vortex core from the presence of the particle within the ring which will be discussed further in the next section.

IV. DYNAMICS OF VORTEX RING INTERACTING WITH BUBBLE/PARTICLE

In this section, we present results from the vortex dynamics side of the interaction with the bubble (and particle), and again focus our attention on the differences between the deforming bubble case (We > 0) and the particle (We $= 0$). In particular, we shall present results on the ring's radial growth and deformations, its propagation speed, and the azimuthal vorticity distribution within the cores during the interaction.

A. Ring growth and deformation

A vortex ring while propagating may slow down due to the growth of the ring's radius due to the entrainment of additional ambient fluid into it, which can lead to the ring's momentum being shared with increased fluid mass. To understand this, in the present paper, we measure the effects of the deforming bubble (We > 0) and particle (We=0) on the ring's radial growth in terms of its increasing (equivalent) diameter (D_{ring}) and, simultaneously, we measure the deformation of the ring quantified in terms of the ring's instantaneous aspect ratio. In the top-view visualization of the interaction, we see that the asymmetric perturbation caused by the bubble (particle) on the ring can cause a deformation of the ring into an elliptical one with subsequent oscillatory axis switching deformations usually seen in elliptic rings. We use the deformed ring perimeter to define an equivalent circular ring diameter (D_{ring}) with the same perimeter as the deformed ring. In Figs. 8(a) and 8(b), the (equivalent) diameter and the aspect ratio of the vortex ring are shown with time at two Re (6000 and 25 800) for both the base and deforming bubble (particle) interaction cases. In Fig. 8(a), this equivalent diameter (D_{ring}) normalized by the ring's initial diameter ($D_{\text{ring},O}$) just before bubble capture, is shown with time (tu_{co}/R_o). In this plot, the growth of the base vortex ring's diameter is found to be around 10% as seen at a later time $tu_{co}/R_o \approx 25$, in both Reynolds numbers, with the laminar one growing slightly more due to the larger viscous diffusive entrainment of ambient fluid, as discussed by Maxworthy [57] and Sullivan *et al.* [58]. In contrast, the presence of bubble or particle in the laminar case is seen to lead to a drastic increase in the ring diameter ($D^*_{\text{ring}}=D_{\text{ring}}/D_{\text{ring},O}$) as compared to the base case. As observed in the plot, the deforming bubble increases D^*_{ring} significantly more compared to the particle, which is likely due to the bubble spreading within the ring, and thereby enhancing viscous diffusion induced entrainment. Assuming the ring holds a constant impulse, as the ring grows bigger, the momentum is shared with more fluid, which would result in a reduction of the rings velocity as discussed in the next subsection. In the turbulent ring case, although there is again an increase in diameter, it is much smaller than the laminar cases.

In bubble and particle-ring interactions, we see that the laminar ring is deformed and takes an elliptic shape. In contrast, the turbulent interacting rings and of course the base ring cases are seen to remain nearly circular (aspect ratio, $\beta \approx 1$). To characterize this, we present in Fig. 8(b) the

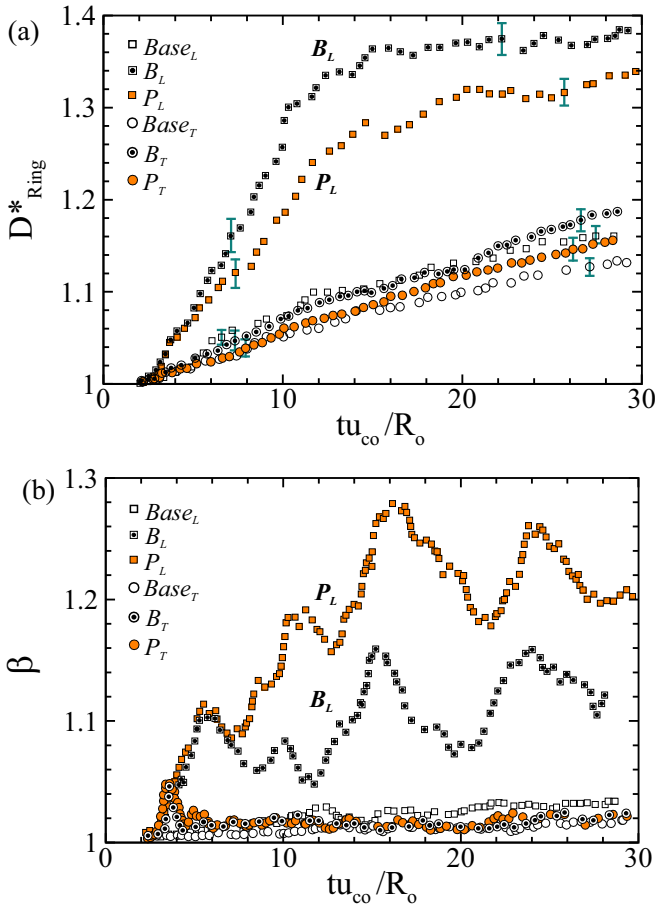

FIG. 8. (a) The variation of the ring-equivalent nondimensional diameter (D^*_{ring}) with nondimensional time (tu_{co}/R_o). Here, D^*_{ring}=$D_{\text{ring}}/D_{\text{ring},O}$; D_{ring} is ring's instantaneous diameter and $D_{\text{ring},O}$ is the diameter before bubble (particle) capture. (b) The variation in aspect ratio (β) of the ring with nondimensional time (tu_{co}/R_o). In these plots, both the base and interaction cases are shown for a laminar (Re=6000) and turbulent (Re=25 800) ring. Here, rigid particle (***P***) and deforming bubble (***B***) cases are subscripted by ***L*** and ***T***, representing a laminar and a turbulent case, respectively.

variation with time of the aspect ratio (β) of the ring, which we define as the instantaneous ratio of the major (D_{major}) to minor (D_{minor}) axis of the deformed vortex ring. As we can see in the figure, in laminar (Re=6000) cases, both the bubble and particle deform the ring making the aspect ratio (β) deviate significantly from unity, with the β being larger for the particle, which as seen earlier acts as a larger asymmetric perturbation to the ring as compared to the bubble that spreads azimuthally within the ring. In the turbulent ring (Re=25 800) case, no noticeable ring deformation is found to occur, except for a relatively small deformation ($\beta \approx 1.05$) at the time of particle (bubble) capture at $tu_{co}/R_o \approx$2.5. In the large deformation laminar Re cases, it is to be noted that the aspect ratio does not remain fixed and fluctuates with time, which can affect the ring's propagation speed. Also, it may be noted that such oscillatory deformation of the vortex ring can help enhance ambient fluid mass entrainment into the ring as discussed by Husain and Hussain [59], thus slowing down the ring's convection speed as the ring's momentum is shared with the increased entrained fluid mass. The significant differences in the vortex ring's growth and deformation between the low (Re=6000) and large (Re=25 800) ring Reynolds number cases could possibly be thought of as the influence

TABLE II. Table shows the buoyant energy contribution from the bubble (particle) as a percentage of the vortex ring's energy, at different ring Reynolds numbers.

Re	Bubble $E_{\text{buoyant}}/E_{\text{ring}}$ (%)	Particle $E_{\text{buoyant}}/E_{\text{ring}}$ (%)
6000	9.06	8.98
13200	5.55	5.51
25800	3.78	3.75
39900	1.64	1.63
56700	0.87	0.86
67300	0.61	0.60

of the buoyancy of the bubble (particle) relative to the vortex ring energy. To understand this aspect, we have calculated the energy (E_{ring}) of the base vortex ring at different Re using the relation from Fraenkel [41], and also calculated the bubble (particle)s buoyant energy (E_{buoyant}) contribution to the vortex ring during its stay within the vortex ring in all the interaction cases. In Table II, the buoyant energy as a percentage of the ring's energy [$E_{\text{buoyant}}/E_{\text{ring}}$ (%)] presented for different Re cases shows that the buoyant energy contribution at Re of 6000 and 25 800 are ≈9% and ≈4% of the ring energy, which, although different, is not very large. Despite there being no considerable difference in buoyancy relative to a ring's energy between these two Re cases, there are still large differences between these two cases in terms of the ring's growth and deformation. This indicates that, rather than buoyancy, the transition of the ring may play a more critical role here.

To summarize this part, we have observed that at low ring Re, the interaction of the ring with the bubble or particle leads to a large increase in the ring diameter with significant oscillatory deformations in shape. More importantly, between the bubble and particle cases, the increase in the equivalent ring diameter by the bubble is more than the particle. On the other hand, the ring deformation (aspect ratio) is larger in the case of the particle, which appears to be related to the very asymmetric perturbation caused by the particle as compared to the bubble that spreads azimuthally within the ring. The resulting oscillatory deformations of the ring can enhance ambient fluid entrainment into the ring, thus slowing down the ring's propagation speed as will be discussed in the next subsection. In contrast, at large Re, in both the deforming bubble and particle (rigid bubble) interaction cases, the ring's diameter and aspect ratio broadly remain similar to the base ring case.

B. Propagation of vortex ring

In bubbly turbulent flows, the presence of the dispersed phase can attenuate the propagation of the coherent structures, which in turn modulates the turbulence [61]. In the present subsection, we try to understand and contrast the role of bubble's deformability on the ring's propagation for a large range of ring strengths (Re). So far, we have seen the comparison between the rigid particle (We=0) and deforming bubble (We > 0) on vortex ring dynamics, including its growth and deformation, which are likely to have an effect on the ring's convection speed. We present in Fig. 9(a) the nondimensional vertical position (z/R_o) as a function of time for the vortex ring as it interacts with the bubble (or particle) at two vortex ring Reynolds numbers (Re) of 6000 and 25 800. In Fig. 9(a), our base (without bubble or particle) laminar and turbulent ring position with time data is seen to collapse and also shows a good match with the model from Fukumoto and Moffatt [60], represented by the thick dashed line. The interacting case data in the plot includes the entire time of interaction between the vortex ring and the bubble (particle), starting from the particle's (bubble's) entrainment into the ring, the particle's azimuthal drift and bubble's azimuthal expansion and breakup; and, lastly, as seen in some cases, the particle (broken) bubbles escaping from the ring (seen at low Re of 6000). It may be noted that the data shown for each of the cases, as shown in Fig. 9(a), are

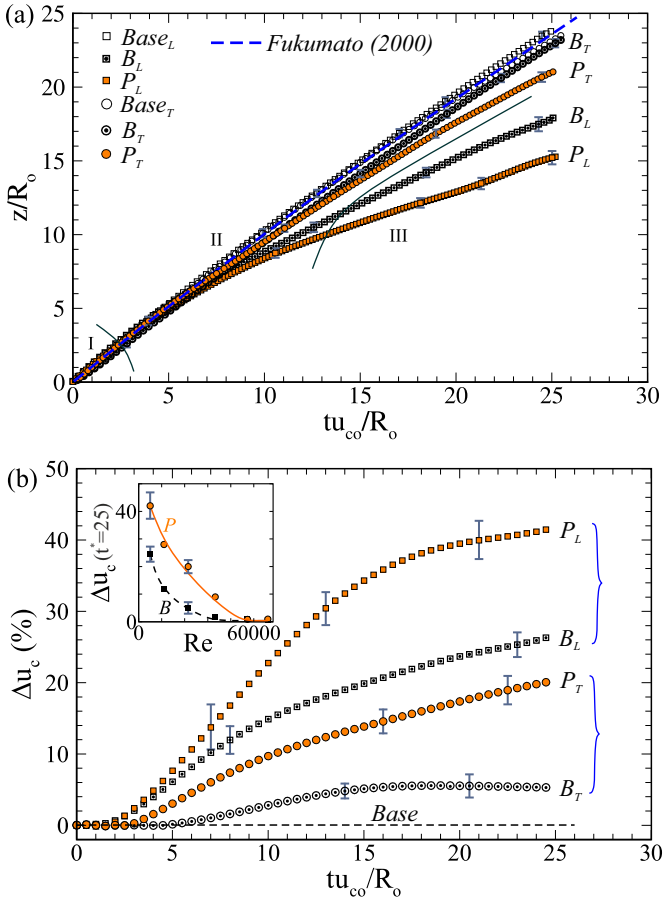

FIG. 9. (a) The nondimensional vertical position ($z^*=z/R_o$) of the vortex ring with nondimensional time ($t^*=tu_{co}/R_o$) shown for laminar (Re=6000) and turbulent (Re=25,800) ring base cases and interaction cases with both bubble and particle. The blue dashed line represents the base ring's position obtained from the viscous vortex ring model [60] and shows a good match with the experimental base ring position data. (b) The percentage reduction in ring's convection speed (Δu_c) with nondimensional time (tu_{co}/R_o) shown for Re=6000 and 25 800, cases. Here, the reduction in convection speed is calculated as $\Delta u_c(\%) = 100 \times (u_{c_{\text{base}}} - u_{c_{\text{interact}}})/u_{c_{\text{base}}}$; here, $u_{c,\text{base}}$ and $u_{c,\text{interact}}$ are the base and interaction case ring's instantaneous convection speed. In the subplot, Δu_c (%) obtained at t^* of 25 is shown for all Re cases studied. In these plots, rigid particle (***P***) and deforming bubble (***B***) are subscripted by ***L*** and ***T***, and these represent the laminar and turbulent ring cases, respectively.

obtained from an average of more than three independent runs, with variation between runs being indicated by uncertainty bars, which is found to be within $\approx 0.5R_o$. Also marked in Fig. 9(a) are different bubble dynamics events or stages of interaction, as discussed in Jha and Govardhan [33], to help correlate the ring dynamics to the bubble dynamics discussed earlier, in particular, the initial interaction referred to as stage I, where the bubbles (particles) are outside the vortex ring, with the capture time indicated by the dashed line demarcating stages I and II. Following the capture of the bubble (particle), in stage II, the bubble undergoes elongation and breakup within the ring and produces a number of smaller bubbles. Finally, another line demarcates the transition to stage III, where the particles (broken bubbles) are seen leaving the vortex cores.

One of the most striking features seen in Fig. 9(a) is the difference between the ring's position in bubble and particle cases at both low Re (6000) and high Re (25 800) cases. At a relatively large ring

Re of 25 800, in the interaction cases, the ring's vertical location (z/R_o) in the case of the interacting bubble case is relatively close to that of the base case, while in the interacting particle case, there is a more significant reduction in the ring's speed. These effects are further amplified in the lower Re of the 6000 ring case. As seen in the plot, both the particle and bubble cause a significant drop in the convection speed of the ring, as seen at later times, with the reduction in the particle case being larger than the bubble. This again indicates that the particle is having a larger impact on the vortex ring dynamics as compared to the bubble. In this lower ring Re, the significant reduction in the ring's convection speed is due to the ring being highly perturbed by the bubble and the particle. To help understand this, in the next subsection, we will present and discuss the modulation of the azimuthal core vorticity and enstrophy of the ring by the bubble and the particle.

For a better illustration of the comparison of the deforming bubble (We >0) and rigid particle (rigid bubble, We=0), the percentage reduction in the ring's convection speed (Δu_c) as compared to the base ring cases is calculated with time and shown in Fig. 9(b). Here, the reduction is calculated as $\Delta u_c(\%)=100 \times (u_{c,\text{base}} - u_{c,\text{interact}})/u_{c,\text{base}}$, where $u_{c,\text{base}}$ and $u_{c,\text{interact}}$ are the base case and interaction case ring's instantaneous convection speed. In this plot, Δu_c for the base ring cases is presented by the solid thick dashed black line, which corresponds to Δu_c of zero for the entire time. Now, focusing on the interaction cases, we can see that the bubble (and particle) reduces the laminar ring's propagation more than the turbulent case, and more importantly, given a ring Re, the particle causes a larger reduction than the bubble. At a later time of $tu_{co}/R_o=25$, the Δu_c is measured for particle and bubble interaction cases for the entire range of ring Re of 6000 to 67 300 studied in the present paper, and this is plotted with Re in the subplot in Fig. 9(b). In this subplot, we can see a drastic increase in Δu_c with decrease in Re from large Re values, with a clear contrast between the bubble and particle cases. It can be seen that at low and intermediate Re, Δu_c for the particle case is higher than the bubble. On the other hand, at very large Re (at about Re $\geqslant$40 000), the ring's convection speed remains nearly unaffected by both bubble and particle, and hence, we find that in these cases Δu_c is approximately zero. Along with the growth in the ring diameter and the deformation of the vortex ring as already discussed, the slowing down of a vortex ring seen is likely also affected by the modified vorticity distribution of the vortex core caused by modifications to the ring core due to the presence of the bubble (particle), which will be discussed in the next subsection.

C. Azimuthal vorticity

The vortex ring's propagation speed is an integral effect of the vorticity distribution within it, and hence, in this section we contrast the similarities and differences between the deforming bubble and rigid particle (rigid bubble) cases in terms of their effects in modifying the vorticity within the core. We present the time sequence of the principal azimuthal vorticity fields ($\omega R_o/u_{co}$) of the vortex ring obtained using 2D time-resolved PIV for the case of bubble and particle at vortex ring Re of 6000 and 25 800 in Figs. 10 and 11, respectively. In both figures, the bubble and particle are marked as a hatched area with a magenta color, and the rigid particle case is shown on the left and the deforming bubble case on the right. In these plots, at an early time, as seen in the first instant in all cases, the bubble (particle) are outside the vortex ring. Following this, they are captured by the low pressure within the core and the interaction begins, as seen in the subsequent time instances, with clear modifications noticeable in the core caused by the bubble (particle) by the last time instant, especially in the laminar case in Fig. 10(a).

We shall now contrast the particle and bubble cases in more detail by specifically discussing the lower Re of 6000 case in Fig. 10, where the effects on the ring are significantly more than at larger Re as seen in previous sections. As we can see, both the particle [in Fig. 10(a)] and bubble [in Fig. 10(b)] modifies the core vorticity significantly at later times ($tu_{co}/R_o = 13$), with the particle and bubble distorting and breaking the vortex core, with the distortion of the core being significantly larger in the particle case. It is to be noted that by this time, the convection speed of the vortex ring (discussed earlier) has substantially decreased compared to the base ring. As we can see in these plots, the rigid

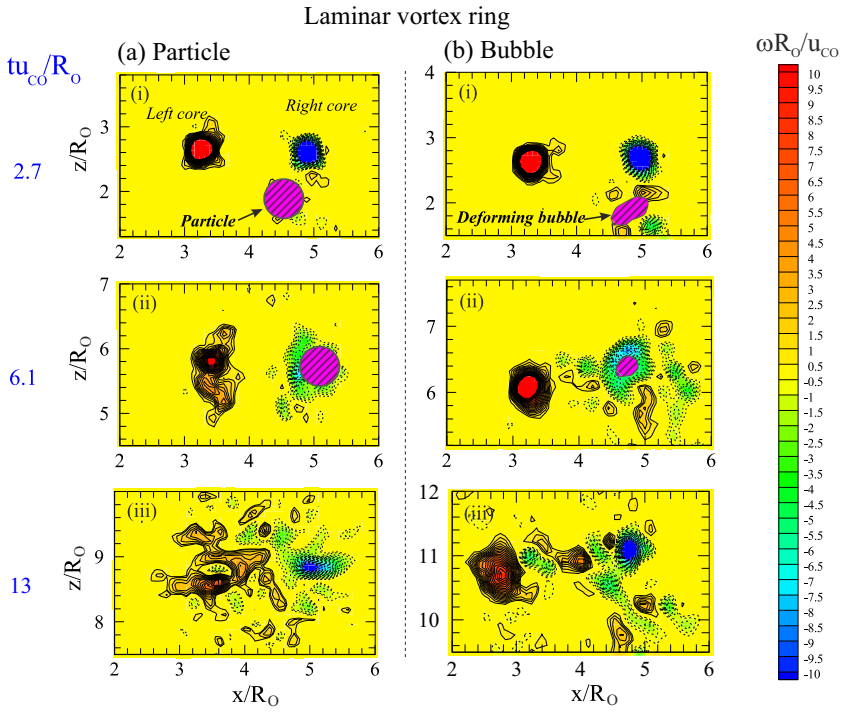

FIG. 10. Comparison of the time sequence of nondimensional azimuthal vorticity ($\omega R_o/u_{co}$) for the interaction of (a) particle and (b) bubble with a laminar (Re=6000) vortex ring. In each image, the particle (bubble) is marked as a hatched area (magenta online). Here, solid and dashed line contours represent positive and negative vorticity, respectively. The nondimensional time (tu_{co}/R_o) corresponding to each of the images are 2.7, 6.1, and 13, as shown on the left side. The nondimensional azimuthal vorticity contour levels are shown on the right.

particle seems to reduce the vortex core's peak vorticity more than the deforming bubble. This may be explained by the fact that the bubble immediately after capture by the ring elongates azimuthally within the ring, thereby resulting in the bubble's cross-sectional area, reducing locally as seen in the shadowgraphy image in Fig. 4(b)(II)(iii). This stretched-out bubble is also visible in the right vortex core in the vorticity field in Fig. 10(b)(ii), along with the modifications to the core vorticity distribution. As the bubble spreads within the vortex core, this results in a smaller local bubble to core diameter ($D_{\text{elong}}/2a_o \approx 0.4$) compared to the particle, which has a larger value of $D_{\text{elong}}/2a_o$ which remains constant at $D_b/2a_o$. Hence, the particle acts as a localized large perturbation to the vortex core and disrupts the core more than the bubble. The resulting broken core loses its coherence, and the pressure within the core is no longer low enough to hold the bubble (or particle), and so they leave the ring. We want to emphasize here that Sridhar and Katz [29] also observed vortex distortion in their study, but the vortex core regained its initial undistorted state in that case once the bubble escaped the vortex core. On the other hand, in our case, the effect of the bubble (particle) on the vortex core is a more lasting one and, as we can see, the core is left in a permanently fragmented state even after the escape of the bubble (particle).

Such breakup of coherent structures by bubbles (particles) in turbulent flows has been observed by Sugiyama *et al.* [12]. In their bubbly Taylor-Couette flow drag reduction study, Sugiyama *et al.* [12] observed that at low Re, microbubbles could perturb and break the coherent structures, which in turn could lead to reduction in overall drag. Jacob *et al.* [22] also showed that the characteristic dimension and coherence of the near-wall coherent vortices are reduced by microbubbles (rigid)

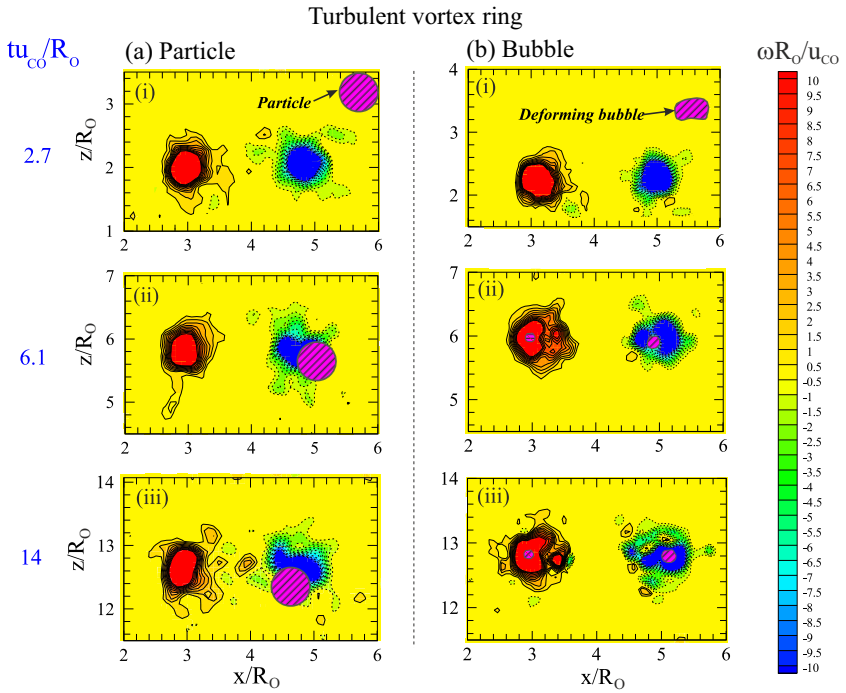

FIG. 11. Comparison of the time sequence of nondimensional azimuthal vorticity ($\omega R_o/u_{co}$) for the interaction of (a) particle, and (b) bubble with a turbulent (Re=25 800) vortex ring. The nondimensional time (tu_{co}/R_o) corresponding to each of the images are 2.7, 6.1, and 14, as shown on the left side. All other markings are as in Fig. 10.

and leads to a reduction in skin friction drag. The recent study by Zhao *et al.* [62] on turbulence modulation by microbubbles (rigid) reported that the near-wall streak intensity is reduced due to the presence of bubbles and, subsequently, the structures become indistinct. All these studies discuss suppression of coherent structures by bubbles which are much smaller than the vortical structures. In the present idealized study where the bubble is of the order of the vortex, we observe that the vortex is perturbed and disrupted more by a rigid bubble (We=0, an asymmetric perturbation) than a deforming bubble (We $>$ 0, a distributed perturbation). The present observation thus indicates that in low Re bubbly turbulent flow drag reduction, where vortex disruption is the primary mechanism for turbulence attenuation (drag reduction), rigid bubbles could disrupt vortices more efficiently than deforming bubbles, and could lead to larger attenuation of turbulence, and hence greater drag reduction.

At the higher ring Re of 25 800 shown in Fig. 11, the vorticity field time sequence in the particle (bubble) cases show that the vortex core remains broadly intact, with a relatively larger core deformation by the particle compared to the bubble, which as explained earlier is related to the fact that the bubble azimuthally expands and hence has a lower local $D_{\text{elong}}/2a_o$ compared to the particle. In these cases, as we have already seen in Fig. 9(b), the reduction in the vortex ring's convection speed Δu_c is smaller compared to the lower Re cases, showing that the convection speed of the ring is much less affected by the bubble compared to the particle, and hence is closer to the base ring case. These observations in our idealized study indicate that at large Re turbulent flows, a bubble's deformability or lack of it would not make any considerable difference to the disruption of the intense vortical structures present in the flow and hence turbulence attenuation through this mechanism would not be an effective one. In such cases, other mechanism(s) would be dominating for turbulence attenuation (and/or drag reduction). This is broadly consistent

with previous studies, for example, Taylor-Couette (TC) flow drag reduction (flow Re=10^3–10^4) Sugiyama *et al.* [12], Murai *et al.* [14], Spandan *et al.* [23], where they have reported that with increasing Re, the structures remain nearly undisrupted by the perturbation induced by the bubbles, and hence turbulence attenuation and drag reduction (DR) requires other mechanisms. At very large Re (Re≈10^5–10^6) TC flows, the dominating DR mechanism is related to the deformations of the larger bubbles (larger than Kolmogorov scale) pushing the near-wall high vorticity regions away from the wall [25].

To summarize this section, we have seen that a rigid bubble (We=0) can disrupt the vortex core more than a deforming bubble (We $>$ 0) due to its local larger bubble to vortex core diameter ratio ($D_b/2a_o$) as compared to the deforming bubble, which has a smaller $D_{\text{elong}}/2a_o$ due to its elongation within the vortex core. This larger disruption of the vortex ring by the rigid bubble reflects in a higher reduction in the ring's convection speed, as seen in Fig. 9.

D. Azimuthal enstrophy

As the convection speed of the vortex ring is an integral effect of its vorticity distribution, hence, one way to look at the physics behind the reduction of convection speed is to investigate the azimuthal enstrophy. In our case, the azimuthal enstrophy of the vortex ring is measured by taking an area integral of ω over a large area ($E=\int \omega^2\, dA$) around both cores as seen in Fig. 10, to cover all the vorticity in the core. We begin here by presenting in Fig. 12 the azimuthal enstrophy [in (a) and (b)] and circulation [in (c) and (d)] as a function of time for a typical particle- (bubble-)ring interaction case at Re of 6000 (laminar), along with the corresponding base cases. The azimuthal vorticity contours in this Re, at different times, have already been shown in Figs. 10(a) and 10(b). Here, the azimuthal enstrophy (E) is normalized by its initial value (E_o), just before the bubble (particle) capture, and, similarly, the circulation (Γ) is normalized by the initial circulation (Γ_o). We can see the transient nature of he left core (LC), right core (RC), and both core averaged (BC) nondimensional azimuthal enstrophy (E/E_o) and nondimensional circulation (Γ/Γ_o) at Re of 6000. In the interaction cases, the capture of the bubble (particle) takes place at tu_{co}/R_o of about 2.5 and, after the capture, there is a large drop in enstrophy [in Figs. 12(a) and 12(b)]; this being observed for both cores. This drop in enstrophy after the capture of the bubble (particle) by the ring results due to a sharp drop in peak vorticity within the vortex core due to the presence of the large bubble (particle) at the center of the core. Following this, as the bubble elongates in the axial (along the core) direction, azimuthal vorticity again increases, and hence the azimuthal enstrophy also increases (as discussed in Jha and Govardhan [33]). This happens in the relatively short timescale of capture and the subsequent axial elongation of the bubble. This present enstrophy increase mechanism is different from Foronda-Trillo *et al.* [37], where it is attributed to the vortex destabilization triggered by the engulfment of vorticity from the bubble. On the other hand, in the particle case in the present paper, immediately after capture, there is a drop in peak core vorticity, and unlike in the bubble case, as there is no azimuthal elongation of the particle, the peak vorticity keeps dropping (seen in both left and right core, see Fig. 10), resulting in a steady reduction in azimuthal enstrophy, while circulation remains nearly the same as the base case. It can be noticed in the figure that immediately after bubble (particle) capture, the reduction in enstrophy in the right core where the capture takes place, is higher than the left core. However, with increasing time, this difference becomes lesser, and at later time ($tu_{co}/R_o \approx$15), the reduction in both the left and right cores are nearly the same, indicating that the bubble (particle) affects the ring nearly uniformly at later time. Further, as seen in Fig. 12, at a later time ($tu_{co}/R_o \approx$15), the base case has about 10% reduction ($E/E_o \approx 0.9$) in azimuthal enstrophy. The interaction cases have much larger reduction in enstrophy, with the reduction being more for the particle case ($\approx$ 80% reduction from base case) compared to the bubble case ($\approx$ 60% reduction compared to the base case).

We have already observed in Fig. 10 that as compared to the bubble, in the particle case, there is a larger reduction in core peak vorticity, and vorticity is spread over a relatively larger area. Hence, the azimuthal enstrophy reduction in the particle case is expected to be more than the bubble.

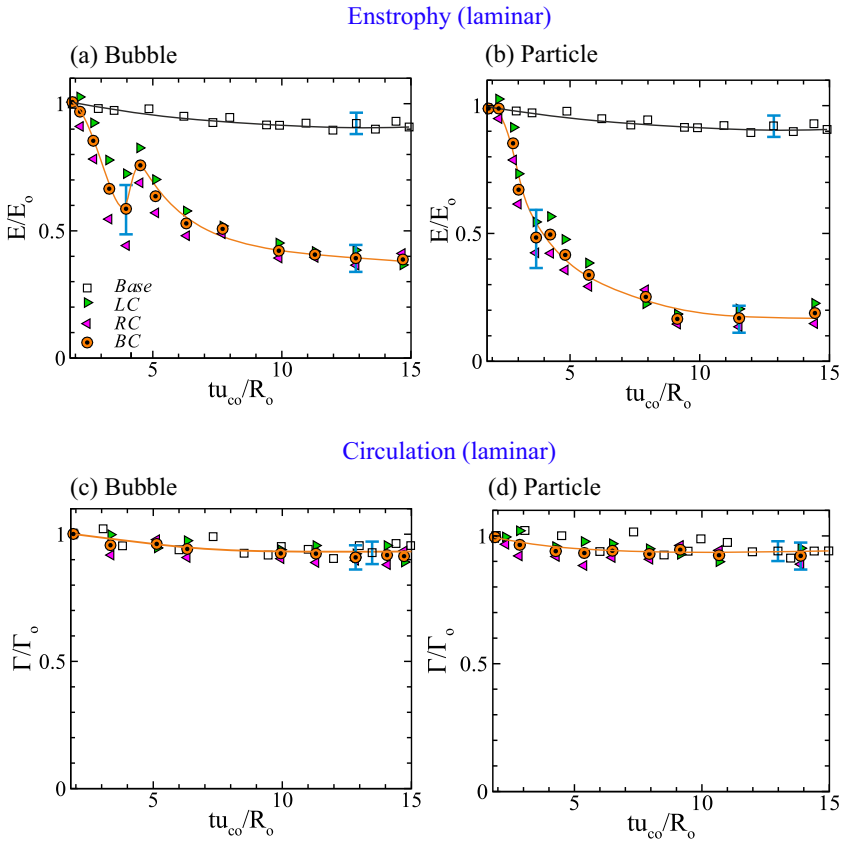

FIG. 12. (a) and (b) show the nondimensional azimuthal enstrophy (E/E_o) with nondimensional time (tu_{co}/R_o) for the bubble and particle, respectively, at laminar Re=6000. Here, instantaneous enstrophy (E) is normalized by the enstrophy (E_o) before the bubble (particle) capture. (c) and (d) show the nondimensional circulation (Γ/Γ_o) with nondimensional time (tu_{co}/R_o) for the bubble and particle, respectively, at laminar Re=6000. Here, the instantaneous circulation (Γ) is normalized by the circulation (Γ_o) before bubble (particle) capture. In these plots, the enstrophy and circulation are shown for the left core (LC), right core (RC), and average of both cores (BC).

These differences between the deforming bubble (We $>$ 0) and rigid particle (We=0) enstrophy can be linked to the larger local $D_{\text{elong}}/2a_o$ ($=D_b/2a_o \approx 1.4$) in a particle acting as a localized large perturbation on the ring as compared to the bubble having a smaller $D_{\text{elong}}/2a_o$ (≈ 0.4), and leading to a larger reduction of the ring's azimuthal enstrophy by the particle than the bubble. In these cases, it should be noted that the average azimuthal enstrophy of both cores is reasonable close to that of the left or right core, and hence may be seen as representative of the azimuthal enstrophy in the entire ring volume. Apart from azimuthal enstrophy, as we also look into the azimuthal circulation of the base and interaction cases with time in Figs. 12(c) and 12(d), we can see that both core circulations are very similar in the interaction cases, and also this is close to the base case. It is also observed that the circulation seems to remain nearly the same in both the base and interaction cases. This indicates that the in-plane vorticity (azimuthal) broadly remains in-plane, and there is no significant transfer of azimuthal vorticity into the out of plane (nonazimuthal) directions. This is an indication that our 2D measurements are representative of the three-dimensional enstrophy of the vortex ring.

To show a broad overview of the final reduction in azimuthal enstrophy for different Reynolds number rings interacting with bubble and particle, we calculate the percentage reduction in az-

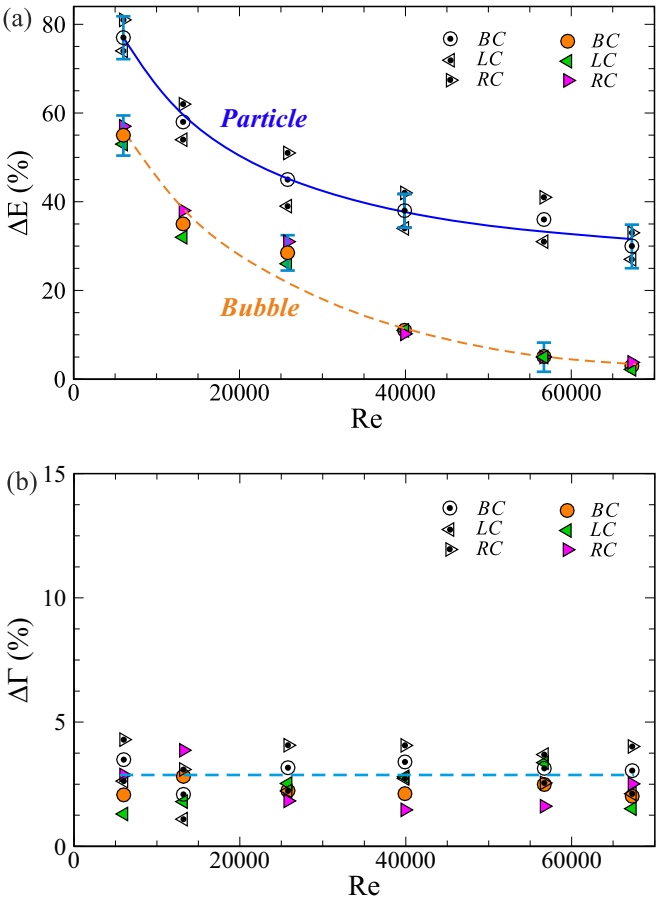

FIG. 13. The variation in the percentage reduction in (a) enstrophy (ΔE) and (b) circulation ($\Delta\Gamma$) at tu_{co}/R_o=15 for bubble and particle cases at all Re studied. Here, the reductions are shown for the left core (LC), right core (RC), and average of both cores (BC).

imuthal enstrophy (ΔE) as compared to the base case, at a later time of $tu_{co}/R_o \approx 15$. In Fig. 13, we report the percentage reduction of azimuthal enstrophy (ΔE) and circulation ($\Delta\Gamma$) at $tu_{co}/R_o \approx 15$ for the left core, right core, and both cores averaged, and plot them with the ring Re. Here, these reductions are calculated, as before, as $\Delta E(\%) = 100 \times (E_{\text{base}} - E_{\text{interact}})/E_{\text{base}}$, and $\Delta\Gamma(\%) = 100 \times (\Gamma_{\text{base}} - \Gamma_{\text{interact}})/\Gamma_{\text{base}}$, where E_{base} and E_{interact} are the base and interaction case azimuthal enstrophy, while Γ_{base} and Γ_{interact} are the base and interaction case circulations, all taken at $tu_{co}/R_o \approx 15$. It can be seen that at low ring Re of 6000, there is a large reduction in enstrophy with $\Delta E \approx 60\%$ for deforming bubble (We > 0) and approximately 80% for the rigid particle (rigid bubble, We=0). With increase in Re, there is reduction in ΔE, and at large Re, ΔE is approximately zero in the bubble case, indicating reduction in enstrophy to be the same as the base case, while for the particle, ΔE is still seen to be considerably large at approximately 30%. In this figure, we can see that for the range of Re studied, nearly 20%–30% difference is there in ΔE between the particle and the bubble. We would like to highlight two facts here. First, comparison of the circulation (in plane) measured in the base ring and the interacting ring case, show that they are nearly the same, indicating that there is no significant reorientation of azimuthal vorticity in nonazimuthal directions (as in Jha and Govardhan [33] and Sridhar and Katz [29]). Foronda-Trillo *et al.* [37] reported azimuthal enstrophy partly getting transferred into nonazimuthal directions, thus reducing

it while the total global enstrophy remained conserved (same as the base case), which does not seem to be happening here. Second, we have measured the azimuthal enstrophy at two diametrically opposite planes (left core and right core) and the measurements again show that the values are not significantly different at any time. These two points taken together, we feel, indicate that the azimuthal enstrophy (core-averaged between the left and right core) is representative of the global enstrophy. The reasons for the differences with the observations in Foronda-Trillo *et al.* [37] are not immediately clear. It should, however, be noted that there are significant differences even in the base vortex ring azimuthal enstrophy between the present results and that of Foronda-Trillo *et al.* [37], with the latter case showing large reduction (approx 60%) in azimuthal enstrophy compared to only about 10% in the present experiments. This and the other differences seen in the interacting cases may be related to the different configuration (parameters) of the ring (bubble), such as transitional ring Reynolds numbers in their numerical study, the different ring nondimensional core thickness (a_o/R_o) between the two cases, and the bubble and vortex rings having large relative velocities (traveling in opposite directions) in their case compared to the lower values in the present case (traveling in the same direction).

To summarize this section, after bubble (particle) capture by the ring, a rigid bubble (We=0) can lead to a higher rate of reduction [see Figs. 12(a) and 12(b)] in the ring's azimuthal enstrophy than a deforming bubble (We $>$ 0) due to its local larger bubble to vortex core diameter ratio as compared to the deforming bubble. At later time, the final reduction in enstrophy is much larger for the rigid bubble compared to the deforming bubble in all the Re cases studied [Fig. 13(a)]. In particular, we note that for high Re rings, the change in enstrophy compared to the base ring case is negligible for a deforming bubble, but is large approximately 30% for the particle. In all cases, the circulation, however, remains nearly constant in both interaction cases, and are very similar to the base cases, thus indicating no significant transfer of azimuthal vorticity into the out-of-plane (nonazimuthal) directions. This along with the fact that there is very little difference between the left and right core enstrophy indicates that a rigid bubble can lead to a higher reduction in the global (volumetric) enstrophy of the ring compared to a deforming bubble.

E. Effects of bubble to vortex size ratio

We have seen at a particular bubble to vortex size ratio of $D_b/2a_o \approx 1.4$ that the bubble deformability and the lack of it in the case of a rigid particle leads to striking differences in the ring convection speed, azimuthal vorticity, and enstrophy. In this subsection, we investigate the effects of the bubble to vortex size ratio ($D_b/2a_o$) on these interactions by varying the bubble (particle) diameter (D_b). In particular, we present results for two other bubble to vortex size ratios ($D_b/2a_o$) of 1.1 and 0.8, which corresponds to We of 9 and 6, respectively, noting that the earlier case of $D_b/2a_o \approx 1.4$ corresponded to a We of 12. All the interactions presented in this subsection correspond to a ring Re of 6000, as the disruption of the vortex by the bubble (particle) is found to be largest at this Re among the cases studied, as discussed in the previous subsections. In these interaction cases for the smaller bubble sizes, as seen from high speed visualizations (not included here), the deformation of the bubble within the vortex ring reduces, as one might expect at lower $\mathrm{We_{bubble}}$, with the bubble remaining nearly spherical within the ring and not breaking up at the lowest $\mathrm{We_{bubble}}$ of 6 case ($D_b/2a_o = 0.8$). Hence, the smallest bubbles are essentially nondeformable like particles. On the vortex ring dynamics side, the final reduction in the convection speed (Δu_c) and azimuthal enstrophy (ΔE) calculated at a later time [similar to Figs. 9(b) and 13(a)] are plotted with $D_b/2a_o$ in Fig. 14. As can be seen, both Δu_c and ΔE reduce as $D_b/2a_o$ is decreased from 1.4 to lower values, with the reduction in both Δu_c and ΔE being larger for the particle at each size. It is, however, clear that as $D_b/2a_o$ is decreased from 1.4, the difference between the bubble and the particle reduces, until at $D_b/2a_o$ of about 0.8, the difference is quite small, and may be expected to tend to zero as the size is further reduced. Thus, the present study on the effects of the bubble to vortex size ratio ($D_b/2a_o$) indicates that as the bubble (particle) size is reduced from larger values of about 1.4, qualitatively the difference between the particle and bubble on the

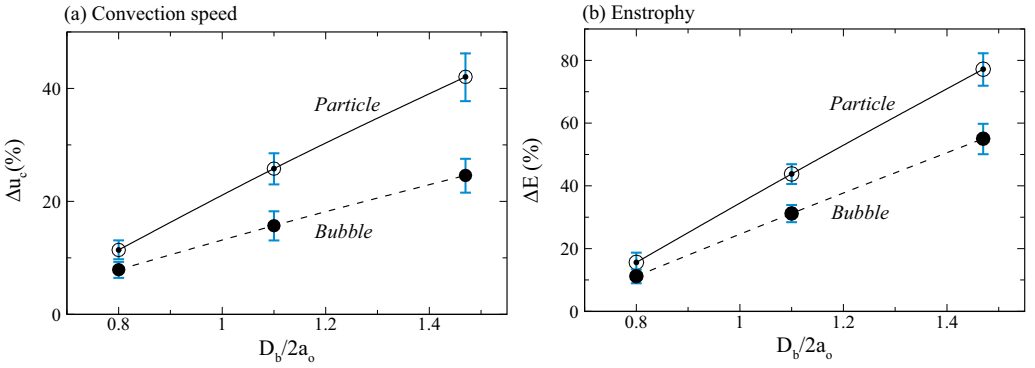

FIG. 14. The variation in the percentage reduction in (a) convection speed (Δu_c), and (b) both core averaged azimuthal enstrophy (ΔE), with $D_b/2a_o$, for bubble and particle cases at Re of 6000. Here, the $D_b/2a_o$ of 1.1 and 0.8 correspond to $\mathrm{We_{bubble}}$ of 9 and 6, respectively.

ring is similar, but as expected the quantitative difference between the bubble and particle cases reduces as the bubble (particle) size becomes smaller. These observations help us to understand the effects of bubble size and its deformability on the dynamics of a vortex ring in vortex-bubble interactions.

V. CONCLUSIONS

We have studied in the present paper an idealized version of the bubble-turbulence interaction problem, focusing specifically on the effect that bubble deformability has on these interactions. In particular, we have studied the interaction of a single deforming air bubble (We $>$ 0) or a rigid buoyant spherical particle (an equivalent of a rigid bubble, We=0) with a single vortex ring, for a wide range of ring Reynolds numbers (Re $\approx$6000–67 300). The novelty of the experiment is that we were able to obtain the particle to fluid density ratio ($\rho_{\mathrm{particle}}/\rho_{\mathrm{water}}$ $\approx$0.008) to be very low and of the same order as that of the bubble ($\rho_{\mathrm{bubble}}/\rho_{\mathrm{water}}$ $\approx$0.001), with the main difference being the distinct difference in their deformability. In particular, we measure the motions of the deforming bubble (rigid particle) directly using high-speed visualizations, while the flow field information is obtained using time-resolved PIV.

In these interactions, the bubble's deformability is seen to lead to striking differences in both the bubble (particle) dynamics and vortex ring dynamics. The interaction begins with the capture process, during which, the bubble undergoes large deformation (elongation) and takes a nonspherical shape, thus experiencing a smaller drag, leading to a nearly 50% lower capture time of the deforming bubble compared to that of the spherical buoyant particle. Postcapture, inside the ring, the deforming bubble shows a variety of engaging dynamics such as elongation, breakup, coalescence, and spread of broken bubbles along the ring circumference, whereas a rigid particle remains intact within the ring undergoing only small azimuthal drifting motions. Within the vortex core, the azimuthally elongated bubble results in a smaller local bubble to core diameter, $D_{\mathrm{elong}}/2a_o$ $\approx$0.4, compared to a particle having a larger value, $D_b/2a_o \approx 1.4$. Hence, the rigid particle (a rigid bubble) acts as a localized large perturbation to the vortex core, while the deformable bubble act as a distributed perturbation to the ring.

On the vortex ring dynamics side, the observed differences in bubble (particle) dynamics leads to distinct differences in the ring's convection speed, azimuthal vorticity, and enstrophy at later times. In particular, the deformation of the ring and the disruption of the vortex cores is more extensive by the particle as compared to the deforming bubble. This is shown clearly by the higher reduction in azimuthal enstrophy of the ring for the particle case, about 80% reduction at Re $\approx$ 6000, compared to the about 60% reduction in the bubble case at the same ring Re. Correspondingly, the

particle causes a larger drop in the ring convection speed (≈40% reduction) compared to that of the deforming bubble (≈25% reduction). At higher ring Re, the changes in convection speed of the ring due to interactions with the bubble (particle) become smaller compared to the base case, although distinct differences are still present in the azimuthal vorticity and enstrophy between the bubble and the particle interaction cases. This is highlighted by the difference in enstrophy between the bubble and the particle interaction cases at high ring Re ≈ 70 000, which shows that the enstrophy is close to the base case for the deforming bubble case, while it continues to be significantly lower than the base case, by approximately 30%, for the interacting particle case.

These observations in our idealized study have several implications in connection to bubbles' deformability in turbulent flows. For example, the capture of a deforming bubble by a vortical structure is much faster than for a nondeforming bubble due to the much lower drag of the elongated (deformed) bubble, which could lead to higher accumulation of deforming bubbles in vortical regions as compared to nondeforming bubbles. Hence, deformable bubbles will have larger probability of interactions with vortical structures. On the other hand, postcapture, rigid bubbles disrupt the vortical structures more efficiently than deforming bubbles. This observation, in connection with BDR, implies that when the disruption of vortical structures is the dominating mechanism for drag reduction, rigid bubbles would disrupt and break the coherent structures more efficiently than deforming bubbles, and thereby lead to a larger reduction in drag. One more example would be bubbly mixing layers where rigid bubbles could disrupt large-scale coherent structures more efficiently, and this could result in differences in the lateral migration and spreading rate of the shear layer between deforming and nondeforming bubble cases.

In summary, in bubbly turbulent flows, the modulation of the vortical structures by bubbles would be influenced by both the bubble's capture probability and the interaction (postcapture) between bubbles and vortices, both being dependent on the bubble's deformability. These broad observations in connection with bubbly turbulent flows could bring us more insight into the role of the bubble's deformability in its interaction with a vortical structure, which could be important in helping us model and understand bubble-turbulence interactions.

[1] S. Balachandar and J. K. Eaton, Turbulent dispersed multiphase flow, Annu. Rev. Fluid Mech. **42**, 111 (2010).
[2] V. Mathai, D. Lohse, and C. Sun, Bubbly and buoyant particle–laden turbulent flows, Annu. Rev. Condens. Matter Phys. **11**, 529 (2020).
[3] S. L. Ceccio, Friction drag reduction of external flows with bubble and gas injection, Annu. Rev. Fluid Mech. **42**, 183 (2010).
[4] S. Elghobashi, Direct numerical simulation of turbulent flows laden with droplets or bubbles, Annu. Rev. Fluid Mech. **51**, 217 (2019).
[5] Y. Murai, Frictional drag reduction by bubble injection, Exp. Fluids **55**, 1773 (2014).
[6] J. Lu and G. Tryggvason, Effect of bubble deformability in turbulent bubbly upflow in a vertical channel, Phys. Fluids **20**, 040701 (2008).
[7] C. Martínez-bazán, J. Montanes, and J. C. Lasheras, On the breakup of an air bubble injected into a fully developed turbulent flow. part 1. breakup frequency, J. Fluid Mech. **401**, 157 (1999).
[8] F. Risso and J. Fabre, Oscillations and breakup of a bubble immersed in a turbulent field, J. Fluid Mech. **372**, 323 (1998).
[9] B. Bunner and G. Tryggvason, Effect of bubble deformation on the properties of bubbly flows, J. Fluid Mech. **495**, 77 (2003).
[10] S. Dabiri, J. Lu, and G. Tryggvason, Transition between regimes of a vertical channel bubbly upflow due to bubble deformability, Phys. Fluids **25**, 102110 (2013).
[11] E. A. Ervin and G. Tryggvason, The rise of bubbles in a vertical shear flow, J. Fluids Eng., Trans. ASME **119**, 443 (1997).

[12] K. Sugiyama, E. Calzavarini, and D. Lohse, Microbubbly drag reduction in Taylor-Couette flow in the wavy vortex regime, J. Fluid Mech. **608**, 21 (2008).
[13] I. M. Mazzitelli, D. Lohse, and F. Toschi, On the relevance of the lift force in bubbly turbulence, J. Fluid Mech. **488**, 283 (2003).
[14] Y. Murai, H. Oiwa, and Y. Takeda, Bubble behavior in a vertical Taylor-Couette flow, in *Journal of Physics: Conference Series* (IOP Publishing, Japan, 2005), Vol. 14, p. 018.
[15] K. Yoshida, Y. Tasaka, Y. Murai, and T. Takeda, Mode transition in bubbly Taylor-Couette flow measured by PTV, in *Journal of Physics: Conference Series* (IOP Publishing, Japan, 2009), Vol. 147, p. 012013.
[16] T. H. van den Berg, S. Luther, D. P. Lathrop, and D. Lohse, Drag Reduction in Bubbly Taylor-Couette Turbulence, Phys. Rev. Lett. **94**, 044501 (2005).
[17] I. M. Mazzitelli, D. Lohse, and F. Toschi, The effect of microbubbles on developed turbulence, Phys. Fluids **15**, L5 (2003).
[18] T. H. van den Berg, S. Luther, and D. Lohse, Energy spectra in microbubbly turbulence, Phys. Fluids **18**, 038103 (2006).
[19] E. Climent and J. Magnaudet, Dynamics of a two-dimensional upflowing mixing layer seeded with bubbles: Bubble dispersion and effect of two-way coupling, Phys. Fluids **18**, 103304 (2006).
[20] N. K. Jha, A. Bhatt, and R. N. Govardhan, Effect of bubble distribution on wall drag in turbulent channel flow, Exp. Fluids **60**, 127 (2019).
[21] D. P. Van Gils, D. N. Guzman, C. Sun, and D. Lohse, The importance of bubble deformability for strong drag reduction in bubbly turbulent Taylor-Couette flow, J. Fluid Mech. **722**, 317 (2013).
[22] B. Jacob, A. Olivieri, M. Miozzi, E. F. Campana, and R. Piva, Drag reduction by microbubbles in a turbulent boundary layer, Phys. Fluids **22**, 115104 (2010).
[23] V. Spandan, R. Ostilla-Mónico, R. Verzicco, and D. Lohse, Drag reduction in numerical two-phase Taylor-Couette turbulence using an euler–lagrange approach, J. Fluid Mech. **798**, 411 (2016).
[24] A. Ferrante and S. Elghobashi, On the physical mechanisms of drag reduction in a spatially developing turbulent boundary layer laden with microbubbles, J. Fluid Mech. **503**, 345 (1999).
[25] J. Lu, A. Fernández, and G. Tryggvason, The effect of bubbles on the wall drag in a turbulent channel flow, Phys. Fluids **17**, 095102 (2005).
[26] V. Spandan, R. Verzicco, and D. Lohse, Deformable ellipsoidal bubbles in Taylor-Couette flow with enhanced euler-lagrangian tracking, Phys. Rev. Fluids **2**, 104304 (2017).
[27] J. Magnaudet and I. Eames, The motion of high-Reynolds-number bubbles in inhomogeneous flows, Annu. Rev. Fluid Mech. **32**, 659 (2000).
[28] A. A. Townsend, *The Structure of Turbulent Shear Flow* (Cambridge University Press, New York, 1980).
[29] G. Sridhar and J. Katz, Effect of entrained bubbles on the structure of vortex rings, J. Fluid Mech. **397**, 171 (1999).
[30] A. J. Cihonski, J. R. Finn, and S. V. Apte, Volume displacement effects during bubble entrainment in a travelling vortex ring, J. Fluid Mech. **721**, 225 (2013).
[31] J. Finn, E. Shams, and S. V. Apte, Modeling and simulation of multiple bubble entrainment and interactions with two dimensional vortical flows, Phys. Fluids **23**, 023301 (2011).
[32] A. Ferrante and S. E. Elghobashi, On the effects of microbubbles on Taylor-Green vortex flow, J. Fluid Mech. **572**, 145 (2007).
[33] N. K. Jha and R. Govardhan, Interaction of a vortex ring with a single bubble: Bubble and vorticity dynamics, J. Fluid Mech. **773**, 460 (2015).
[34] S. Biswas and R. N. Govardhan, Effect of single and multiple bubbles on a thin vortex ring, J. Flow Visualization Image Process. **27**, 1 (2020).
[35] S. Biswas and R. N. Govardhan, Effects of weber number on the interaction of single and multiple bubbles with a vortex ring, in *APS Division of Fluid Dynamics Meeting Abstracts* (American Physical Society, Chicago, 2020), pp. J10–010.
[36] S. Biswas and R. N. Govardhan, Interaction of a vortex ring with single and multiple air bubbles, in *APS Division of Fluid Dynamics Meeting Abstracts* (American Physical Society, Seattle, 2019), pp. G28–004.
[37] F. Foronda-Trillo, J. Rodrguez-Rodrguez, C. Gutirrez-Montes, and C. Martnez-Bazn, Deformation and breakup of bubbles interacting with single vortex rings, Int. J. Multiphase Flow **142**, 103734 (2021).

[38] T. Uchiyama and H. Yagami, Numerical simulation for the collision between a vortex ring and solid particles, Powder Technol. **188**, 73 (2008).
[39] K. Domon, O. Ishihara, and S. Watanabe, Mass transport by a vortex ring, J. Phys. Soc. Jpn. **69**, 120 (2000).
[40] J. Norbury, A family of steady vortex rings, J. Fluid Mech. **57**, 417 (1973).
[41] L. E. Fraenkel, Examples of steady vortex rings of small cross-section in an ideal fluid, J. Fluid Mech. **51**, 119 (1972).
[42] J. Choi, C.-T. Hsiao, G. Chahine, and S. Ceccio, Growth, oscillation and collapse of vortex cavitation bubbles, J. Fluid Mech. **624**, 255 (2009).
[43] M. Gharib, E. Rambod, and K. Shariff, A universal time scale for vortex ring formation, J. Fluid Mech. **360**, 121 (1998).
[44] A. Glezer, The formation of vortex rings, Phys. Fluids **31**, 3532 (1988).
[45] J. P. Sullivan, S. E. Widnall, and S. Ezekiel, Study of vortex rings using a laser doppler velocimeter, AIAA J. **11**, 1384 (1973).
[46] M. K. Tripathi, K. C. Sahu, and R. Govindarajan, Dynamics of an initially spherical bubble rising in quiescent liquid, Nat. Commun. **6**, 6268 (2015).
[47] S. Takagi and Y. Matsumoto, Surfactant effects on bubble motion and bubbly flows, Annu. Rev. Fluid Mech. **43**, 615 (2011).
[48] R. Clift, J. R. Grace, and M. E. Weber, *Bubbles, Drops, and Particles* (Academic Press, New York, 1978).
[49] S. Takagi, T. Uda, Y. Watanabe, and Y. Matsumoto, Behavior of a rising bubble in water with surfactant dissolution: 1st report, steady behavior, Trans. Japan Soc. Mech. Eng. **69**, 2192 (2003).
[50] P. Duineveld, The rise velocity and shape of bubbles in pure water at high Reynolds number, J. Fluid Mech. **292**, 325 (1995).
[51] Y. Tagawa, S. Takagi, and Y. Matsumoto, Surfactant effect on path instability of a rising bubble, J. Fluid Mech. **738**, 124 (2014).
[52] R. Mei, J. F. Klausner, and C. J. Lawrence, A note on the history force on a spherical bubble at finite Reynolds number, Phys. Fluids **6**, 418 (1994).
[53] G. Oweis, I. Van der Hout, C. Iyer, G. Tryggvason, and S. Ceccio, Capture and inception of bubbles near line vortices, Phys. Fluids **17**, 022105 (2005).
[54] W. L. Haberman and R. Morton, An experimental investigation of the drag and shape of air bubbles rising in various liquids, technical report, David Taylor Model Basin, Washington, D.C., 1953.
[55] A. Hölzer and M. Sommerfeld, New simple correlation formula for the drag coefficient of non-spherical particles, Powder Technol. **184**, 361 (2008).
[56] S. Biswas and R. N. Govardhan, Bubble capture, breakup, and coalescence in vortex–bubble interaction, in *Proceedings of 16th Asian Congress of Fluid Mechanics* (Springer, Singapore, 2021), pp. 33–41.
[57] T. Maxworthy, Some experimental studies of vortex rings, J. Fluid Mech. **81**, 465 (1977).
[58] I. S. Sullivan, J. J. Niemela, R. E. Hershberger, D. Bolster, and R. J. Donnelly, Dynamics of thin vortex rings, J. Fluid Mech. **609**, 319 (2008).
[59] H. S. Husain and F. Hussain, Elliptic jets. Part 3. Dynamics of preferred mode coherent structure, J. Fluid Mech. **248**, 315 (1993).
[60] Y. Fukumoto and H. Moffatt, Motion and expansion of a viscous vortex ring. Part 1. A higher-order asymptotic formula for the velocity, J. Fluid Mech. **417**, 1 (2000).
[61] M. Pang, J. Wei, and B. Yu, Numerical study on modulation of microbubbles on turbulence frictional drag in a horizontal channel, Ocean Eng. **81**, 58 (2014).
[62] P. Zhao, Y. Chen, G. Dong, Y. Liu, and X. Lyu, Proper orthogonal decomposition analysis on longitudinal streaks in channel flow laden with micro-bubbles, Fluid Dyn. Res. **51**, 035504 (2019).